A Phase Transformation Enthalpy Parameter for Modeling Quench Hardening of Steels

AUGUSTINE SAMUEL, K.M. PRANESH RAO, and K. NARAYAN PRABHU

The effect of phase transformations on the steel/quenchant interfacial heat flux during quench hardening heat treatment is investigated in the present work. Experimental and modeling approaches comprising the inverse heat conduction problem (IHCP) were employed to analyze the thermal behavior of different steel grades with varying section thicknesses. The results revealed that phase transformation led to a distinctive pattern of the interfacial heat flux, characterized by a dip and subsequent rise. We observed that increasing the section thickness increases the surface heat flux for stainless steel probes without phase transformation. In contrast, the surface heat flux decreased with thicker sections in phase transformation. The increased heat evolved due to the latent heat liberation during phase transformation, and a reduction in thermal diffusivity due to increased specific heat caused a fall in the heat flow rates. Furthermore, the study proposed a phase transformation enthalpy parameter (ΔQ) to access the enthalpy change during quenching. ΔQ was consistent for a specific steel grade and independent of section thickness but varied with the cooling rate or quench media. The incorporation of phase transformation in the quenching heat transfer model is complex due to the required material data, including TTT/CCT diagrams and thermophysical properties that vary with steel grade. The study suggests directly incorporating the ΔQ values into the heat conduction equation or the IHCP model with phase transformation, simplifying the simulation process and minimizing data inputs. A database on ΔQ as a function of temperature and cooling rate would facilitate heat transfer modeling during quench hardening.

I. INTRODUCTION

THE quench hardening process in steels encompasses a complex interconnected phenomenon, incorporating various factors such as heat transfer from the steel to the quenching medium, the evolution of microstructure, and the development of stress and strain within the quenched component.[1] These three phenomena occur concurrently and are intricately linked to each other. The heat transfer from the steel surface to the quenching medium is of particular significance, which plays a critical role in determining the resulting microstructure and stress levels in the material. By regulating the heat transfer or the cooling rate of the component, it becomes possible to modify the microstructure and mechanical properties of the steel. Employing simulation techniques for quench hardening allows for evaluating heat transfer rates, temperature distribution within the component, microstructure, and mechanical properties. Consequently, quenching simulation proves valuable in optimizing process parameters and selecting appropriate quenchants to attain the desired microstructure and mechanical properties, while minimizing residual stress and distortion in the component.[2,3]

In the quenching process, a heated metal specimen in its austenitized state is rapidly submerged into a liquid quenching medium maintained at a lower temperature. The dissipation of heat from the metal surface to the liquid medium is a multiphase phenomenon and takes place in a series of three stages, known as the film boiling, nucleate boiling, and convective cooling stages.[4] In film boiling stage, also referred to as the vapor blanket stage, it involves the formation of a vapor blanket surrounding the metal as soon as the heated metal is rapidly immersed into the liquid media. The heat extracted from the surface of the quenched part exceeds the heat required to vaporize the liquid quenchant. During this phase, a stable vapor film envelops the quenched part, and heat transfer primarily occurs through radiation from the metal surface and conduction within the vapor film. Due to the vapor film acting

AUGUSTINE SAMUEL, K.M. PRANESH RAO, and K. NARAYAN PRABHU are with the Department of Metallurgical and Materials Engineering, National Institute of Technology Karnataka, Surathkal, Mangalore, Karnataka, 575025 India. Contact e-mail: knprabhu@nitk.edu.in

as an insulator, the heat transfer rate at this stage is relatively low.[5] The vapor film eventually ruptures when the surface temperature reaches the Leidenfrost or rewetting temperature, which marks the transition from vapor blanket to nucleate boiling. In the second stage, *i.e.*, the nucleate boiling stage, the liquid medium in contact with the quenched part's surface undergoes boiling, generating numerous small bubbles on the surface. As the fluid coming in contact with the metal surface evaporates, the bubbles are driven upward by gravity, leading to a highly efficient convection heat transfer process. It is during this stage that the maximum heat transfer is achieved. In the convective cooling stage, the temperature of the metal surface remains below the boiling point of the liquid medium. The liquid quenchant exists as a single phase, and heat transfer takes place through conduction and convection driven by the fluid's thermo-migration. However, the heat transfer rate at this stage is notably lower in comparison with the other stages.[6,7]

The transition from film to nucleate boiling stage occurs through the rupture of vapor film leading to a direct contact of the liquid medium with the heated metal surface. Therefore, the transition process is also known as the rewetting phenomena.[8] The rewetting phenomena can occur in two ways: (i) Newtonian type of rewetting where the vapor film ruptures in a very short duration or in an explosive manner, and (ii) non-Newtonian rewetting, where vapor film rupture and subsequent rewetting occurs over a long duration of time. The rewetting is affected by many factors such as the component geometry, presence of oxide layer on the surface or surface deposition, immersion pressure, and locally differing immersion periods.[9]

In the non-Newtonian type of rewetting, the transition from film boiling to nucleate boiling stage does not occur uniformly/instantaneously over the entire sample surface; instead, it happens over a period of time by forming a local wetting front. Usually, with a cylindrical sample, wetting front initiates at the bottom of the specimen as it is the first portion to cool and ascends toward the top. As a result, the film boiling and nucleate boiling stages are coexisting simultaneously.[10] The magnitude of heat transfer coefficient for nucleate boiling stage is one order higher than film boiling stage. The significant difference in the heat transfer coefficients of film and nucleate boiling stages causes the oscillation in surface temperature leading to steep thermal gradients.[11] The rewetting phenomenon is the primary source of non-uniformity or the spatial variation in heat transfer that leads to non-uniform hardening, residual stress, distortion, and quench cracking.[12] The kinematics of rewetting is assessed by the rewetting time and the wetting front velocity. Rewetting time indicates the time duration for the completion of the rewetting process, whereas the wetting front velocity is the velocity with which the local wetting front ascends from the bottom to the top of the quench probe.[13]

The properties obtained during the quenching process are influenced by the section thickness of the steel being treated. It is widely recognized that larger steel components experience faster cooling at their surface than their interior. This discrepancy in cooling rates gives rise to non-uniform properties within the steel, resulting in higher hardness at the surface in contrast to the core. Therefore, when selecting a suitable quenching medium for the hardening of a particular grade of steel, it is crucial to consider the geometry and section thickness of the steel. Fernandes and Prabhu[14] studied the impact of section size on heat transfer during the quenching process of AISI 1040 steel using water and oil as quenching media. Their findings revealed that the smaller section with a diameter of 28 mm exhibited a higher peak heat flux when quenched in water, whereas the opposite trend was observed when quenched in oil. Specifically, the 44-mm-diameter steel experienced a higher peak heat flux during oil quenching. Grum *et al*.[15] conducted a study investigating the influence of steel mass on the quenching process. They performed experiments using 42CrMo4 steel specimens with a 35 mm diameter and heights of 5 mm and 15 mm. Two different quenching media were used: a 10 pct aqueous polymer solution and a rapid quenching oil. These experiments demonstrated that the larger test piece exhibited more efficient quenching when immersed in the polymer solution than the oil medium.

Ramesh and Prabhu[16] established a correlation between the section thickness of a stainless steel (SS) 304 probe and the cooling rate and the surface heat transfer coefficient. They found that the cooling rate and heat transfer coefficient exhibited a linear relationship for smaller diameter probes. However, as the probe diameter increased, the correlation became exponential. Babu[17] investigated the impact of section thickness on surface heat flux using SS 304 probes of various diameters quenched in water. Nayak and Prabhu[18] conducted a similar study using vegetable oils. As SS 304 does not undergo phase transformation, both studies observed that the heat flux magnitude increased with increased probe diameter or section thickness. Prasanna Kumar[19] examined the influence of steel grade on cooling rates and heat flux transients using AISI 1025 and 4140 steel probes with a diameter of 25 mm. The results indicated that the heat flux is specific to the steel and quenching medium combination.

Accurate measuring or estimating heat flux or heat transfer coefficient at the interface between the steel and the quenching medium is crucial for predicting temperature distribution, microstructure, and mechanical properties. The heat transfer from the steel surface to the quenching medium involves multiple phases, including film boiling, nucleate boiling, and convective cooling.[20] Therefore, accurately replicating the boundary heat flux or heat transfer coefficient is highly complex. In such cases, the inverse heat conduction problem (IHCP) is a valuable tool where the boundary heat flux can be estimated by analyzing the temperature history within the component. The IHCP is an iterative technique that involves arbitrary estimation of the boundary heat flux based on minimizing errors between the measured and calculated temperatures within the quenched component.[21]

Early research on applying the IHCP to estimate the boundary heat flux during casting and quenching was carried out by Das and Paul,[22] Prabhu and Ashish,[23]

and Babu and Kumar.[24] Prasanna Kumar[25] introduced the coupling of a phase transformation model with the IHCP for estimating the heat flux during the quenching of plain carbon and alloyed steels. This model is based on the decomposition of austenite during cooling and involves solving the Johnson–Mehl–Avarami–Kolmogorov (JMAK) equation for diffusion-based transformations and the Koistinen–Marburger (KM) equation for martensitic transformation. The model requires temperature and phase-dependent thermophysical properties, latent heat, and the time–temperature transformation diagram (TTT) as material data. Babu and Kumar[26] compared the heat flux obtained using experimentally determined TTT diagrams as material input with simulated TTT diagrams using various models. The results indicated that the heat flux obtained with published TTT diagrams was more reliable compared to those simulated using models. Nayak and Prabhu[18] estimated the heat flux transients of AISI 1045 and 1090 steel cylinders with 25 and 50 mm diameters while quenching them in sunflower and Karanja vegetable oil quenchants. The surface heat flux exhibited a dip and rise of heat flux, indicating the phase transformation. Simha et al.[27] utilized the IHCP-phase transformation coupled model to predict the hardness of AISI 1025, 1045, 4140, 4340, and 52100 steel cylinders measuring Ø26 mm × 75 mm. The specimens were end-quenched in water, and the predicted hardness values agreed with the measured values.

Estimating heat transfer and thermal field during quenching of steels generally involves using constant thermophysical properties and a constant/temperature-dependent heat transfer coefficient as the boundary condition. To make simulation realistic, the effects of phase transformations and the associated enthalpy changes have to be included.[11] This is particularly important when estimating boundary conditions using Inverse Heat Conduction Problems. To incorporate the effect of phase transformation, additional material data inputs such as the time–temperature transformation (TTT) diagram and thermophysical properties as a function of temperature and phase fraction have to be known. This makes the simulation process more complicated. To avoid this complexity, a novel technique for heat transfer simulation during quench hardening is proposed. A phase transformation enthalpy parameter to characterize the enthalpy changes due to phase transformation during quenching of different grades of steels having varying section thicknesses is presented. A database on the phase transformation enthalpy parameter for different grades of steels could be incorporated in the heat conduction model to predict temperature distribution within the quenched component.

A. Theoretical Background

1. Inverse heat conduction problem (IHCP)

A brief procedure of the IHCP is outlined as follows: Initially, an arbitrary value of heat flux (q) is chosen, such as $q = 1000 \text{W/m}^2$. Utilizing this constant heat flux value, the heat conduction equation is solved for a specified number of future time steps. The objective is to minimize the least square norm $F(q)$ shown in the Eq. [1], which represents the cumulative error between the measured temperature ($Y(t)$) within the probe and the theoretically estimated temperature ($T(r,t)$) at the measured location. The minimization of $F(q)$ involves iteratively adjusting the assumed heat flux value and recalculating the heat conduction equation solution to determine a new least square norm. This iterative process continues until a satisfactory level of convergence is achieved, indicating a close match between the estimated and measured temperatures.

$$F(q) = \sum_{i=1}^{m} \left(Y_{n+i}(t) - T_{n+i}^l(r,t) \right)^2 \qquad [1]$$

The subscripts n, i, and m denote the global time step, future time step, and the total number of future time steps, respectively. On the other hand, the superscript l represents the iteration number.

The estimation of the optimal heat flux value (q) for the nth global time step is achieved through an iterative process that minimizes the least square norm ($F(q)$) with respect to q. To facilitate this minimization, the conjugate gradient regularization method is employed.[28]

The equation below provides the gradient of $F(q)$ with respect to q, represented as $\nabla F(q_n^l)$.

$$\nabla F(q_n^l) = \sum_{i=1}^{m} -2 \frac{\partial T_{n+i}^l}{\partial q_n^l} \left(Y_{n+i} - T_{n+i}^l \right) \qquad [2]$$

The sensitivity coefficient, denoted by J_n^l, is used to represent the term $\frac{\partial T_{n+i}^l}{\partial q_n^l}$ in Eq. [2].

The sensitivity coefficient quantifies the effect of a small change in the heat flux (q_n^l) on the estimated temperature (T_{n+i}^l). The central difference method calculates the sensitivity coefficient, as depicted in Eq. [3]. In this equation, ε represents a small value, typically taken as 10^{-4}, used for the finite difference approximation.

$$J_n^l = \frac{\left(T_{n+i}^l(q_n^l + \varepsilon q_n^l) - T_{n+i}^l(q_n^l - \varepsilon q_n^l) \right)}{2\varepsilon q_n^l} \qquad [3]$$

The heat flux is iteratively updated using the following procedure:

$$q_n^{l+1} = q_n^l - \beta_n^l d_n^l \qquad [4]$$

The search step size, β_n^l, and the direction of descent, d_n^l, are calculated using the following equations:

$$d_n^l = \begin{cases} \nabla F(q_n^l), & l = 1 \\ \nabla F(q_n^l) + \gamma_n^l d_n^{l-1}, & l > 1 \end{cases} \qquad [5]$$

The conjugate coefficient, γ_n^l, is determined by performing the following calculations:

$$\gamma_n^l = \sum_{i=1}^{m} \frac{\left(\nabla F(q_n^l)\right)^2}{\left(\nabla F(q_n^{l-1})\right)^2} \quad [6]$$

Search step size $\beta_n^l = \dfrac{\sum_{i=1}^{m} \left(J_n^l d_n^l\right)\left(T_{n+i}^l - Y_{n+i}\right)}{\sum_{i=1}^{m} \left(J_n^l d_n^l\right)^2}$ [7]

The iterative procedure continues until the following convergence criteria is met:

$$\left|\frac{q_n^{l+1} - q_n^l}{q_n^{l+1}}\right| < 0.005 \quad [8]$$

2. *Finite element solution of heat conduction equation*

A brief description of the finite element solution of the phase transformation coupled heat conduction equation is as follows[1,11,29]:

The one-dimensional heat conduction equation in the cylindrical coordinate system is solved to determine the radial temperature distribution within the probe model. Equation [9] represents the 1D heat conduction equation, which incorporates a heat source term $(\dot{Q})$ to accommodate the evolution of latent heat during phase change.

$$\frac{1}{r}\frac{\partial}{\partial r}\left(kr\frac{\partial T}{\partial r}\right) + \dot{Q} = \rho C_p \frac{\partial T}{\partial t} \quad [9]$$

Throughout the cooling process, the product phases undergo continuous evolution. Therefore, the thermophysical properties (k, ρ, C_p) of the steel are treated as functions of both temperature and phase fraction (ξ_k). The thermophysical properties are evaluated at each time step using a linear mixture rule, as depicted in Eq. [10].

$$P(T, \xi_k) = \sum_{k=1}^{N} P_k \xi_k \quad [10]$$

P_k and ξ_k represent the thermophysical property and volume fraction of the kth constituent phase (austenite, ferrite, pearlite, bainite, and martensite). The rate of internal heat generation $(\dot{Q})$ resulting from latent heat evolution is estimated according to the following expression:

$$\dot{Q} = \sum_{k=1}^{N} \rho_k L_k \frac{d\xi_k}{dt} \quad [11]$$

L_k denotes the latent heat evolved during the transformation from austenite to the kth product phase, measured per unit weight in joules per kilogram (J/kg).

On the other hand, $\left(\frac{d\xi_k}{dt}\right)$ represents the rate of phase transformation for the kth phase.

The phase fractions associated with diffusion-controlled transformations, such as austenite to ferrite, pearlite, and bainite, are determined by utilizing a combination of Scheil's additivity principle and the Johnson–Mehl–Avrami–Kolmogorov (JMAK) equation. Scheil's additive criteria account for the initial incubation period of the transformation. Subsequently, the phase fractions during the growth stage of the transformation are obtained by the JMAK equation. In accordance with Scheil's additive rule, the nucleation stage of the phase transformation is considered complete, or the growth stage commences when Scheil's sum (S) given in Eq. [12] reaches a value of unity.

$$S = \sum_{j=1}^{n} \frac{\Delta t_j}{\tau_s(T_j)} \approx 1 \quad [12]$$

In the equation mentioned above, Δt_j represents the time step increment, and $\tau_s(T_j)$ denotes the isothermal time required for the initiation of transformation at the temperature T_j. The phase fraction of the product phase in the current time step, denoted as $\xi_k^{t+\Delta t}$, is calculated using the JMAK equation, which is presented as follows:

$$\xi_k^{t+\Delta t} = \xi_k^{\max}\left(\xi_\gamma^t - \xi_k^t\right)\left(1 - \exp\left(b_k(T)(\tau + \Delta t)^{n_k(T)}\right)\right) \quad [13]$$

ξ_γ^t represents the phase fraction of austenite at the previous time step while ξ_k^t represents the phase fraction of the product phase at the previous time step. $\xi_k^{\max}$ denotes the maximum volume fraction of the product phase. In the case of complete pearlitic or bainitic transformation, $\xi_k^{\max}$ is equivalent to the volume fraction of austenite available at the start of the transformation. For pro-eutectoid transformation involving ferrite/cementite, $\xi_k^{\max}$ is determined using the lever rule from the equilibrium phase diagram, as illustrated below.

$$\xi_\alpha^{\max} = \begin{cases} 0; & T > A_{e3} \\ \xi_\alpha^{eq}\frac{A_{e3}-T}{A_{e3}-A_{e1}}; & A_{e1} < T < A_{e3} \\ \xi_\alpha^{eq}; & T < A_{e1} \end{cases} \quad [14]$$

$$\xi_\alpha^{eq} = \frac{C_e - C_o}{C_e - C_\alpha} \quad [15]$$

C_e represents the eutectoid carbon composition, which is determined by equating A_{e3} with A_{e1} in the empirical equation and solving for the weight percentage of carbon. C_o denotes the nominal carbon content of the steel. C_α represents the solubility of carbon in ferrite at the eutectoid temperature, which is assumed to be 0.02 wt pct in the current study.

In the JMAK equation (Eq. [14]), τ refers to the fictitious time, which is calculated based on the volume fraction of the kth product phase at the previous time step. τ is incremented by the time step Δt to determine the newly transformed volume fraction.

$$\tau = \left(\frac{-\ln(1 - \xi_k(t))}{b_k(T)}\right)^{\frac{1}{n_k(T)}} \qquad [16]$$

$n_k(T)$ and $b_k(T)$ represent the temperature-dependent time coefficient and exponent, respectively. These coefficients are determined from the time–temperature transformation (TTT) diagram in the following manner:

$$n_k = \frac{\ln\left(\frac{\ln(\xi_{ki}-1)}{\ln(\xi_{kf}-1)}\right)}{\ln\left(\frac{t_i}{t_f}\right)} \qquad [17]$$

$$b_k = -\frac{\ln(\xi_{ki} - 1)}{t_i^{n_k}} \qquad [18]$$

ξ_{ki} and ξ_{kf} represent the phase fractions corresponding to the transformation start (0.1 pct) and transformation end (99.9 pct), respectively. t_i and t_f correspond to the isothermal time required for the start and end of the transformation of a given phase at a specific temperature.

The phase fraction of martensite is calculated using the Koistinen–Marburger (KM) equation, which is presented below:

$$\xi_m = \xi_\gamma(1 - \exp(-\Omega(M_s - T))) \qquad [19]$$

ξ_γ represents the remaining austenite's volume fraction at the beginning of the martensitic transformation. Ω is a constant with a fixed value of 0.011, regardless of the chemical composition of the steel. M_s refers to the martensite start temperature.

The critical transformation temperatures are calculated using empirical equations obtained from the literature. The elemental compositions are given in weight percentage (wt pct).

$$\begin{aligned} A_{e3}(^\circ C) = {} & 883.49 - 275.89C + 90.91C^2 - 12.26Cr \\ & + 16.45CCr - 29.96CMn + 8.49Mo \\ & - 10.80CMo - 25.56Ni + 1.45MnNi \\ & + 0.76Ni^2 + 13.53Si - 3.47Mn\ Si \qquad [20] \end{aligned}$$

$$\begin{aligned} A_{e1}(^\circ C) = {} & 727.37 + 13.40Cr - 1.03CCr - 16.72Mn \\ & + 0.91CMn + 6.18CrMn - 0.64Mn^2 \\ & + 3.14Mo + 1.86CrMo - 0.73MnMo \\ & - 13.66Ni + 0.53C\ Ni + 1.11CrNi \\ & - 2.28MnNi - 0.24Ni^2 + 6.34Si - 8.88CrSi \\ & - 2.34MnSi + 11.98Si^2 \end{aligned}$$

$$[21]$$

$$\begin{aligned} B_S(^\circ C) = {} & 656 - 58C - 35Mn - 75Si - 15Ni - 34Cr \\ & - 41Mo \end{aligned}$$

$$[22]$$

$$\begin{aligned} M_S(^\circ C) = {} & 512 - 453C - 16.9Ni + 15Cr - 9.5Mo \\ & + 217C^2 - 71.5CMn - 67.6CCr \qquad [23] \end{aligned}$$

3. *Finite element formulation of heat conduction equation*

The weighted integral statement of the 1D heat conduction equation is as follows:

$$\int w\left[\frac{k}{r}\frac{\partial T}{\partial r} + k\frac{\partial^2 T}{\partial r^2} + \dot{Q} - \rho C_p \frac{\partial T}{\partial t}\right]dv = 0 \qquad [24]$$

w is the weight function and the elemental volume $dv = dr dz r d\varphi$. Considering radial symmetry of the steel probe, the integration of Eq. [24] reduces to integration only with respect to dr. The finite elemental equation for solving the temperature distribution is of the form:

$$[K]^e\{T\}^e + [C]^e\left(\frac{\partial T}{\partial t}\right)^e = \{F\}^e \qquad [25]$$

where

$$K_{ij}^e = \int kr\left(\frac{\partial \psi_i}{\partial r}\frac{\partial \psi_j}{\partial r}\right)dr \qquad [26]$$

$$C_{ij}^e = \int \rho C_p r \psi_i \psi_j dr \qquad [27]$$

$$F_i^e = \int r\psi_i \dot{Q}dr - r_{max}q|_{r=r_{max}} \qquad [28]$$

The symbol Ψ in the above equations denotes the linear interpolation or shape functions for the 1D line elements.

For solving transient temperature distribution, the Galerkin integration scheme was used. Since the thermophysical properties are a function of temperature and phase fractions, the FE problem is nonlinear. Therefore, the matrices K and F are solved iteratively at every time step. The equation for temporal approximation is shown in Eq. [29].

$$\begin{aligned} & \left(\Delta t\theta[K]_{n+1}^{l+1} + [C]_n\right)\{T\}_{n+1} \\ & = \left([C]_n - \Delta t(1 - \theta)[K]_n\right)\{T\}_n + \Delta t(1 - \theta)\{F\}_n \Delta t\theta\{F\}_{n+1}^{l+1} \end{aligned}$$

$$[29]$$

In the above equation, $\theta = 2/3$, and $\Delta t = 0.1$ s. The equation can be written as a system of simultaneous linear equations, as shown below:

$$[A]\{T\}_{n+1} = \{B\} \qquad [30]$$

where $[A] = \Delta t\theta[K]_{n+1}^{l+1}+[C]_n$ and $\{B\} = ([C]_n - \Delta t(1-\theta)[K]_n)\{T\}_n+\Delta t(1-\theta)\{F\}_n+\Delta t\theta\{F\}_{n+1}^{l+1}$

The initial condition $T(r, t = 0) = 860\,°C$ and the boundary condition $T(r = 0, t) = Tc(t)$ (the measured temperature at the center) are applied. The iterative procedure is stopped when the following end criteria is met:

$$\frac{\left[\sum_{i=1}^{N}\left(T_i^{l+1} - T_i^l\right)^2\right]^{1/2}}{\left[\sum_{i=1}^{N}\left(T_i^{l+1}\right)^2\right]^{1/2}} \leq 10^{-6} \qquad [31]$$

II. EXPERIMENTAL METHOD

A. Materials

The composition of the steels utilized in the study is presented in Table I. The effect of phase transformation on the interfacial heat flux between the metal and quenchant was observed by selecting medium-carbon (AISI 1045) and high-carbon (AISI 52100) steels. The heat flux estimation without phase transformation was conducted using austenitic stainless steel (SS 304). A medium-carbon (AISI 1045) and high-carbon steel (AISI 52100) were chosen, as their phase transformation behaviors differ considerably. The selection of these steels was made with the consideration that the IHCP coupled phase transformation model could be applied to steels with a wide range of carbon content and other alloying elements.

The geometry of the steel probes is depicted in Figure 1. The steel probes had diameters of 12.5, 25, and 50 mm, with heights of 60 mm for the 12.5-mm-diameter probe and 30 mm for the 25 and 50 mm probes, respectively. Two 1-mm-diameter holes were drilled at the center and 2 mm from the surface to enable temperature measurement within the probe, as illustrated in Figure 1. The holes were drilled to the mid-depth of the probe. The quenchants employed were as follows: (i) mineral oil (Chemquench-RQ, Thin-Chemie Formulations, Chennai, India), (ii) agitated mineral oil, and (iii) distilled water. Table II presents the volume of quenchant used for each case. Quenchant volume was determined based on the heat balance equation, as illustrated further.

$$(mC_p\Delta T)_{steel} = (\rho VC_p\Delta T)_{quenchant} \qquad [32]$$

$$\Delta T_{Steel} = (860 - 30) = 830\,°C \qquad \text{and}$$
$$\Delta T_{quenchant} = 6.46\,°C$$

On substituting the various values in the heat balance equation, quenchant volumes are calculated using Eqs. [33] and [34].

$$\text{For mineral oil,} \quad V_{quenchant} = 0.048 m_{steel} \qquad [33]$$

$$\text{For water,} \quad V_{quenchant} = 0.01429 m_{steel} \qquad [34]$$

B. Quenching Experiment

Figure 2(a) illustrates the schematic of the quench setup. The steel probes were heated and austenitized at a temperature of 860 °C, followed by quenching into the liquid media placed beneath the furnace. The quench bath was maintained at room temperature, specifically 30 ± 2 °C. K-type thermocouples were inserted into the steel probe to measure the temperatures at the center and surface during the cooling process. The probe/thermocouple assembly was vertically held using a stainless steel rod in a tubular furnace. The quenching of the probe was carried out manually. The thermocouples inserted in the probe were connected to a data acquisition system (DAQ NI 9213), which recorded the temperature decrease over time during cooling. At least three trials were conducted for each steel/quenchant combination.

In the case of quenching cylindrical specimens, the length-to-diameter ratio (L/D) plays a crucial role in heat transfer. When the L/D ratio exceeds 4, heat transfer through the lateral surface area of the probe becomes significantly greater than through the end faces. Therefore, neglecting or assuming insulation for the heat flow through the end faces in the simulation is possible. However, when the L/D ratio is less than 4, heat transfer through the end faces becomes equally significant to the lateral surface area. Consequently, temperature measurements taken along the radial direction are affected due to substantial heat transfer through the end faces. This makes it difficult to visualize the impact of section thickness on heat transfer. To address this issue, the end faces of the steel probes were insulated using a paste made of zirconia, alumina, and sodium silicate in equal proportions by weight. For the 25 and 50 mm probes, both end faces were insulated by applying the insulating paste and sandwiching it with a thin layer of glass wool. The insulated probes were heated to 180 °C to cure the

Table I. Elemental Composition of Steels[18]

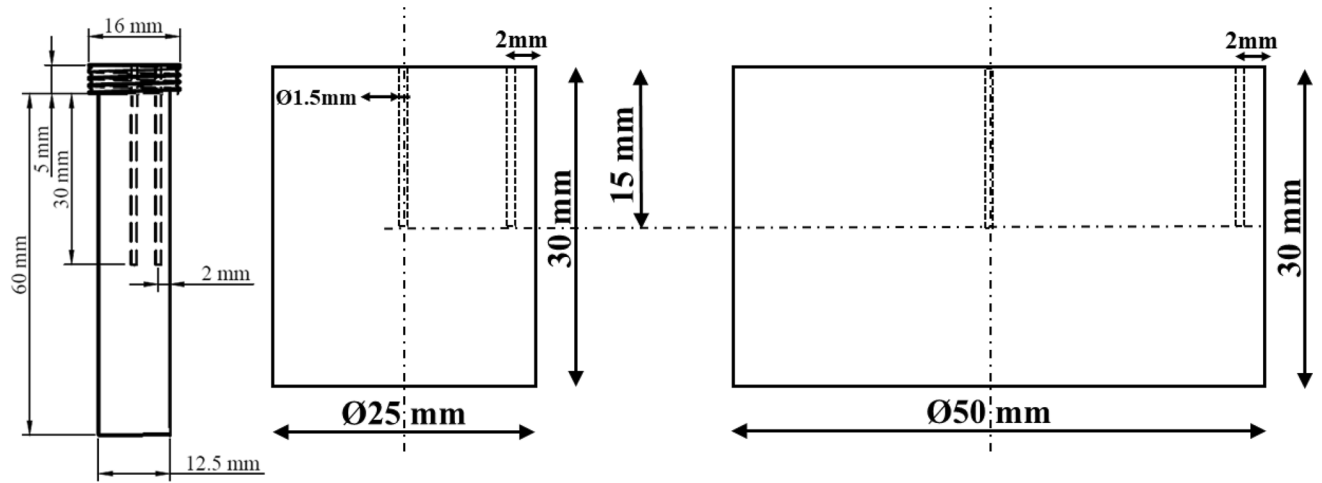| Steel Grade | Elements (Wt Pct) | | | | | | | | |
	C	Mn	Si	Cr	Cu	Ni	S	P	Fe
AISI 1045	0.45	0.7	0.2	—	—	—	0.040	0.040	98.57
AISI 52100	0.96	0.35	0.3	1.4	0.02	—	0.015	0.02	96.935
SS 304	0.08	2	—	19	0.3	9.5	—	—	69.12

Fig. 1—Steel probe geometry (adapted from Ref. [30]).

Table II. Calculated Quenchant Volumes for Various Diameter Probes

	Quenchant Volume (Liters)	
Probe Diameter (mm)	Mineral Oil	Water
12.5	3.36 ≈3.4	1
25	5.76 ≈5.8	1.7148 ≈1.72
50	22.08 ≈ 22.1	6.5734 ≈ 6.6

paste. In the case of the 12.5 mm probe, insulation was not necessary as the L/D ratio exceeded 4. Nayak and Prabhu[18] demonstrated that the insulating paste reduced heat transfer through the end faces by approximately 96 pct. Figure 2(b) shows the probe/thermocouple assembly with the insulated end faces.

C. Examination of Microstructure and Hardness Measurement

The quench-hardened steel probes of AISI 1045 and 52100 were sectioned at a mid-depth. The sectioned surface was polished using various grades of emery sheets before, and velvet cloth polish was performed to obtain a mirror surface finish. The polished surface was etched using 5 pct Nital solution, and the surface was observed under an optical microscope.

The hardness of the quenched steel probes was determined using a Vickers micro-hardness tester. A load of 1 kg and a holding time of 15 seconds were used. The hardness was measured along the radius from the center to the surface of the steel probe.

D. Estimation of Heat Flux Through IHCP Model with Phase Transformation

The program code for heat flux estimation was developed using MATLAB (R2021b). The IHCP algorithm utilizes temperature measurements obtained within the steel probe and employs an iterative algorithm for estimation as explained in Section I–A. Figure 3 displays a 1D model of the steel probe. The probe is considered to be radially symmetric, with the center and surface indicated by the radial locations $r = 0$ and $r = r_{max}$, respectively. The temperature distribution along the probe's radius is calculated using a finite element solution to the 1D transient heat conduction equation. At the surface, denoted as BC1, the boundary condition requires the estimation of the heat flux ($q(t)$). At the center (BC2), which represents a symmetry surface, the heat flux (q) is assumed to be zero, and the measured center temperature ($Tc(t)$) is applied as the boundary condition. To estimate the unknown heat flux ($q(t)$) at BC1, the temperature measurement made at a location of 2 mm from the surface($T(r = r_{max} - 2, t)$) is taken as the reference temperature ($Y(t)$) to solve the IHCP. The 1D model of the probe is discretized using a two-node line element with a length of 0.05 mm.

The steels' thermophysical properties and TTT diagrams are obtained from the JMAT-Pro software (Sente Software Ltd., UK).[31] The temperature and phase-dependent thermophysical properties are shown in Figure 4. The TTT diagrams of AISI 1045 and 52100 steels are shown in Figure 5.

III. RESULTS AND DISCUSSION

A. Cooling Profiles in Steel Cylinders

The measured temperature *vs* time profile of SS 304, AISI 1045, and 52100 steel cylinders, respectively, while quenching in mineral oil is shown in Figure 6. The temperature profiles are measured at 2 mm from the surface of the steel probes and at the geometric center. The cooling curve at the center is used as an essential boundary for the 1D finite element model. In contrast, the surface cooling curve is used as the reference temperature to solve the IHCP to estimate metal/quenchant interfacial heat flux. The temperature profile of SS 304 probes represents the cooling curves without
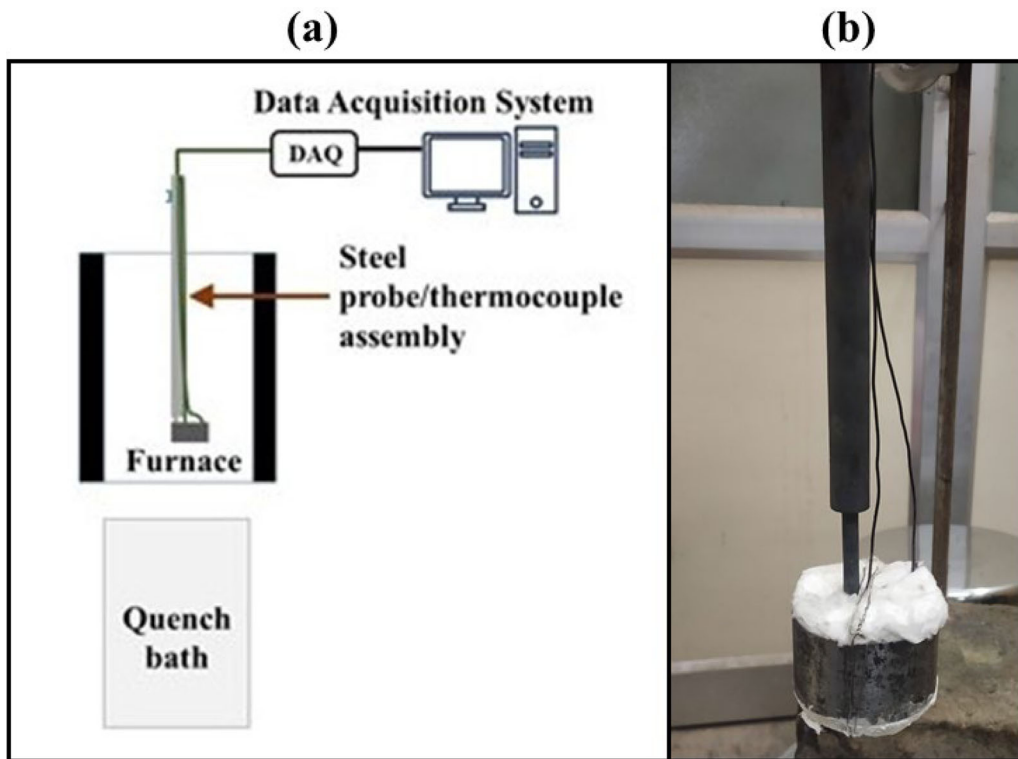
Fig. 2—(*a*) Quench setup, (*b*) steel probe/thermocouple assembly showing insulation on end faces ((a) adapted from Ref. [30]).
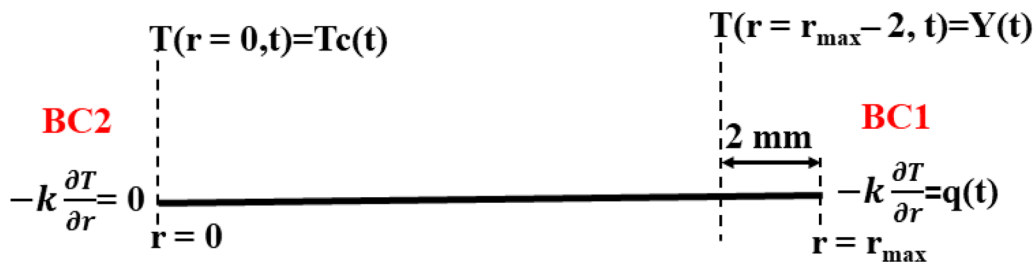

Fig. 3—1D model of steel probe (reprinted from Ref. [30]).

the phase transformation. The occurrence of phase transformation is identified in the cooling curves of 1045 and 52100 steels by the presence of a dip and a rise in temperature during cooling. For higher section thickness specimens (25 and 50 mm), a delayed occurrence of the dip is observed in the center cooling curve compared to the surface, indicating a delayed phase transformation due to an increase in the thermal gradient. The temperature *vs* time/cooling curve data of SS304, AISI 1045, and 52100 steel probes quenched in water and agitated mineral oil are provided in Appendix A1 and A2, respectively. In the case of agitated quench media, only 25- and 50-mm-diameter probes were quenched due to quenchant bath constraint. Agitation was performed using a mechanical stirrer. For the 12.5-mm-diameter probe, only 3.4 liters of mineral oil and 1 liter of water

were used. Accommodating the stirrer was difficult due to the limited volume.

Figure 7 shows the cooling rate *vs* temperature profile at the geometric center and surface while quenching SS 304, AISI 1045, and 52100 steel probes of various section thicknesses in mineral oil. In the cooling rate profiles, the phase transformation or the dip and rise of temperature in the cooling curve data are exaggerated as an inversion in the cooling rate followed by a rise with the decrease in the temperature. The cooling rate data for varying section thicknesses of SS304, AISI 1045, and 52100 steel probes quenched in water and agitated mineral oil, respectively, are shown in Appendix A3 and A4, respectively. For AISI 1045 steel probes, the inversion and rise in the cooling rates are observed for 25- and 50-mm-diameter probes. In the case of 52100
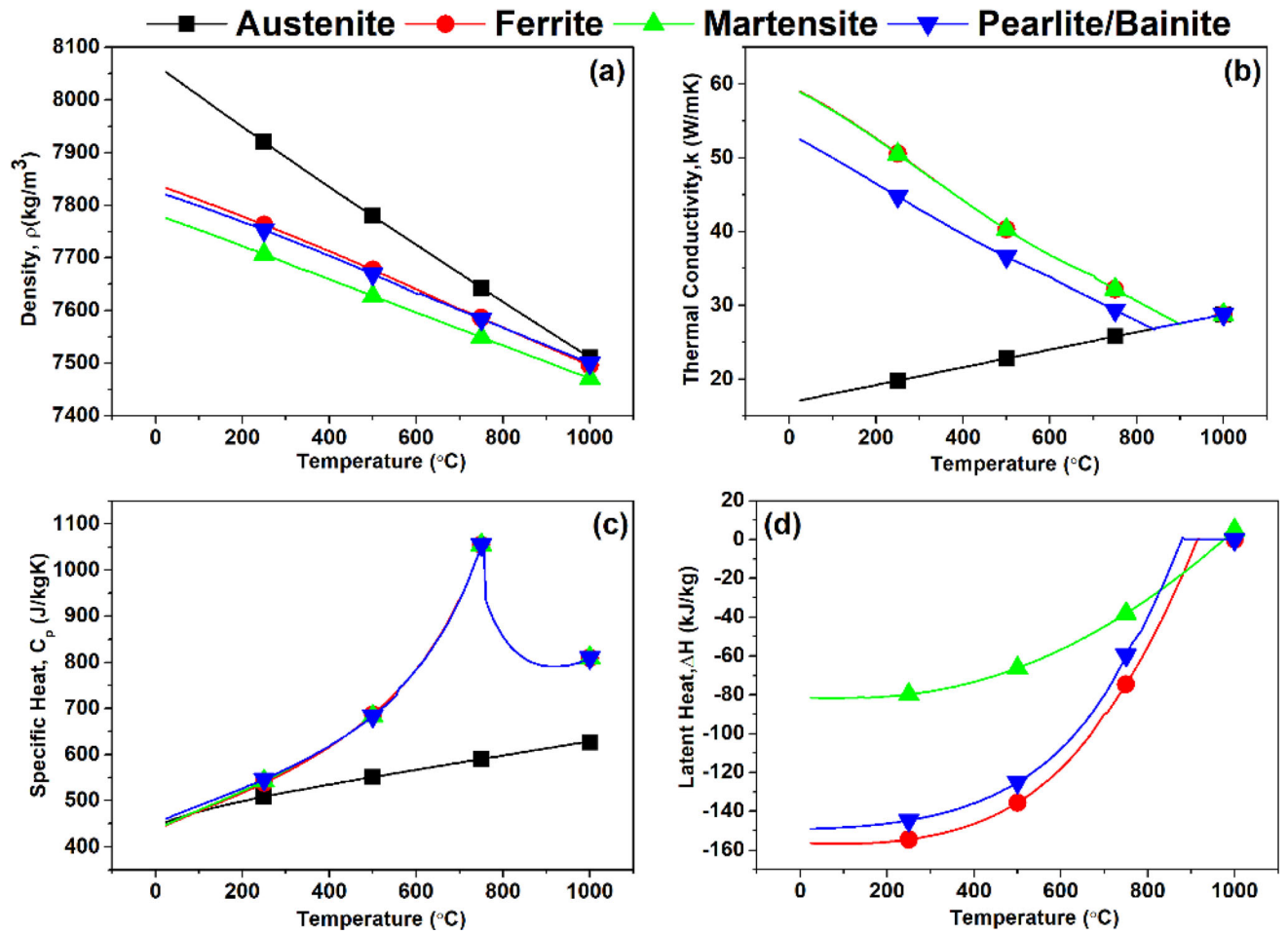
Fig. 4—Thermophysical properties of AISI 1045 steel obtained from JMAT-Pro software: (*a*) density, (*b*) thermal conductivity, (*c*) specific heat, and (*d*) enthalpy change due to phase transformation (reprinted from Ref. [30]).
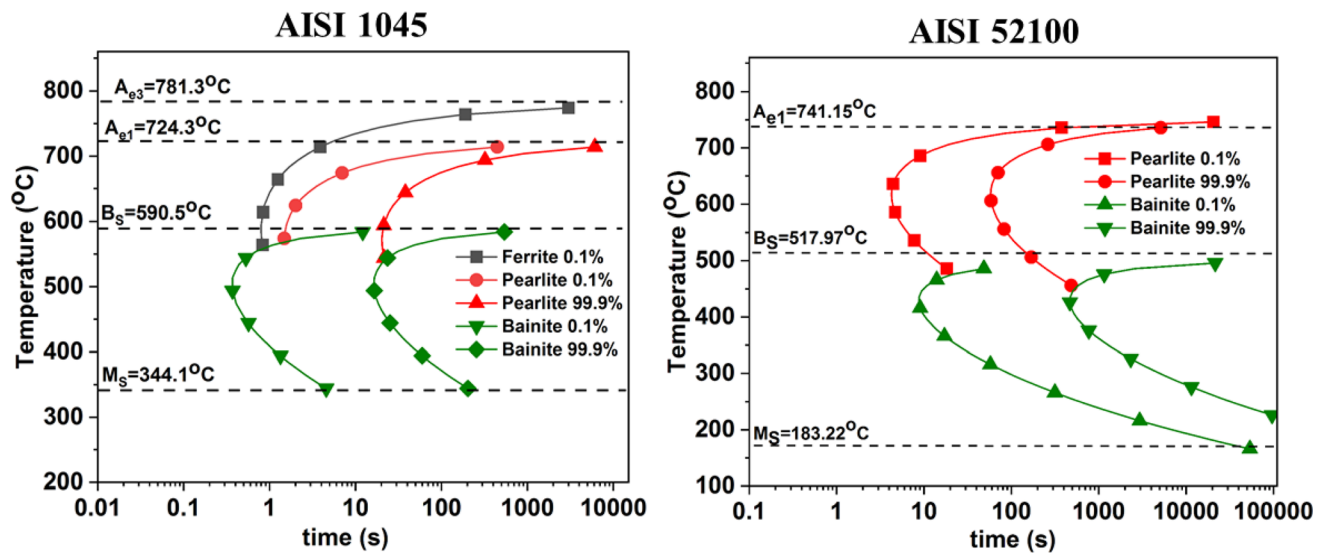

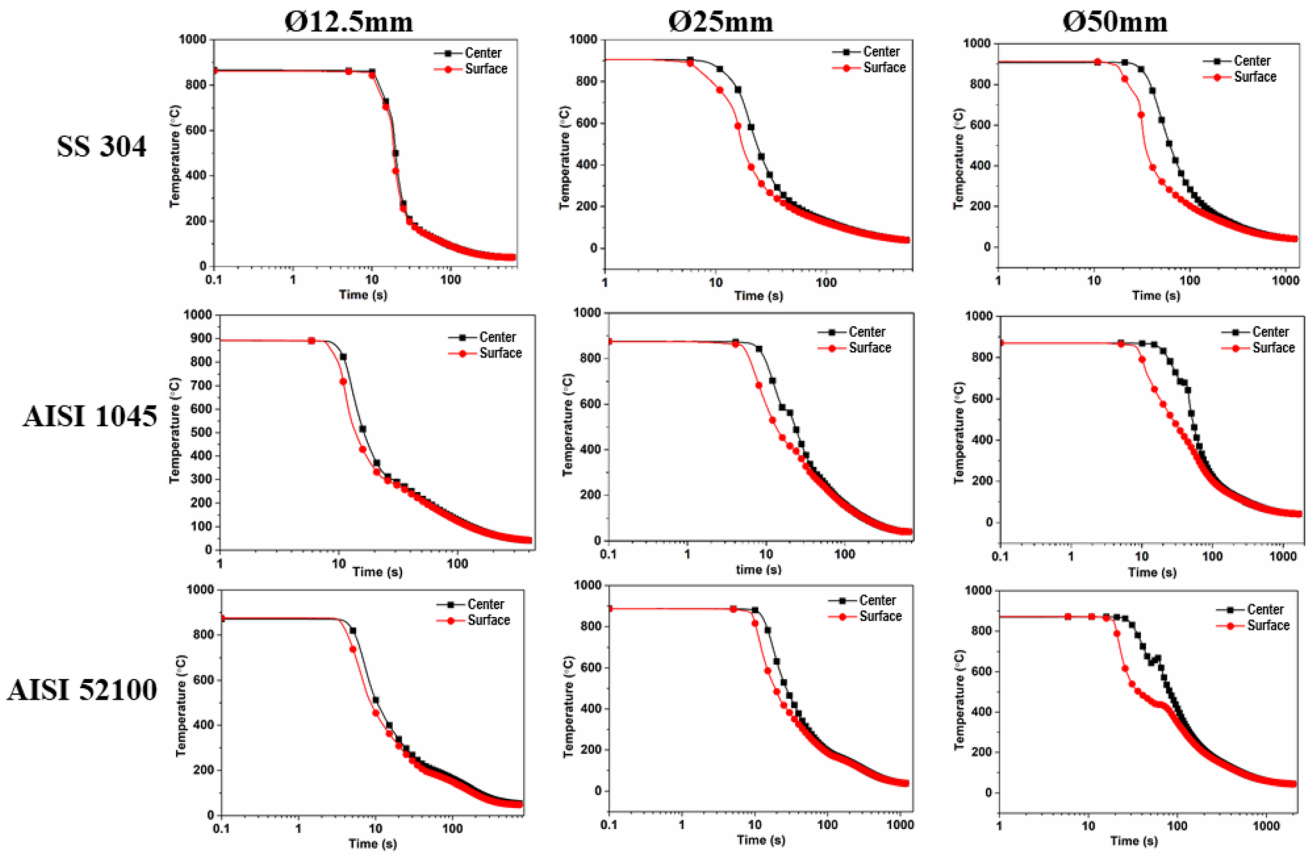Fig. 5—TTT diagrams of steels obtained from JMAT-Pro (reprinted from Ref. [30]).

Fig. 6—Temperature *vs* time profiles measured at the geometric center and 2 mm from the surface of various section thickness SS 304, AISI 1045 and 52100 steel probes, respectively, quenched in mineral oil.

probes, the inversion of cooling rate is observed in a 50-mm-diameter probe indicating substantial phase transformation as compared to 12.5- and 25-mm-diameter probes.

The near-surface cooling curves and cooling rate curves for SS 304 steel, across various section thicknesses, reveal distinct stages of heat transfer at the steel/quenchant interface. The film boiling stage is marked by a plateau region in the cooling curve. In the cooling rate curve, the initial increase in cooling rate followed by a gradual decline suggests the presence of vapor film boiling phenomena. Subsequently, an exponential decrease in the cooling curve and a sudden spike in cooling rate indicate nucleate boiling phenomena. Following this exponential cooling curve decrease and cooling rate rise, the final stage of heat transfer, *i.e.*, the convective cooling, is characterized by the flattening of both the cooling curve and cooling rate curve.

The film boiling was either minimal or was not observed in the surface cooling curves of AISI 1045 and 52100 steels. The SS 304 probes, before use, were conditioned by repetitive heating and quenching in mineral oil. Preconditioning helps form stable and uniform nickel/chromium oxide layers on the surface of the stainless steel probes. The smooth oxide surface of the SS probe favors the vapor film boiling while quenching. It is reflected in the cooling curve profile by forming an initial plateau region before the exponential decrease in the temperature *vs* time plots. In the case of medium- and high-carbon steel probes, heating/austenitizing at a temperature of 860 °C in an ambient atmosphere leads to decarburization and formation of oxide scales at the metal surface. The oxide scales are brittle and break down into smaller pieces while quenching in liquid media due to the boiling phenomena occurring at the steel/quenchant interface. The breaking of oxide scales disrupts the stability of vapor film formation; hence, minimal or no film boiling stage is observed in the cooling profiles.

B. Heat Flux Estimation

The estimated heat flux for SS 304, AISI 1045, and 52100 steel probes of various section thicknesses quenched in mineral oil, water, and agitated mineral oil, respectively, is shown in Figure 8. The heat flux estimated with SS 304 probes indicates the heat flux without phase transformation. The variation in the heat flux is due to the different stages of heat transfer occurring at the steel quenchant interface. The heat flux curve emulates the cooling rate *vs* temperature curves. The initial rise and a plateau region indicate the film boiling stage. The peak region shows the nucleate boiling where maximum heat flux occurs. The end
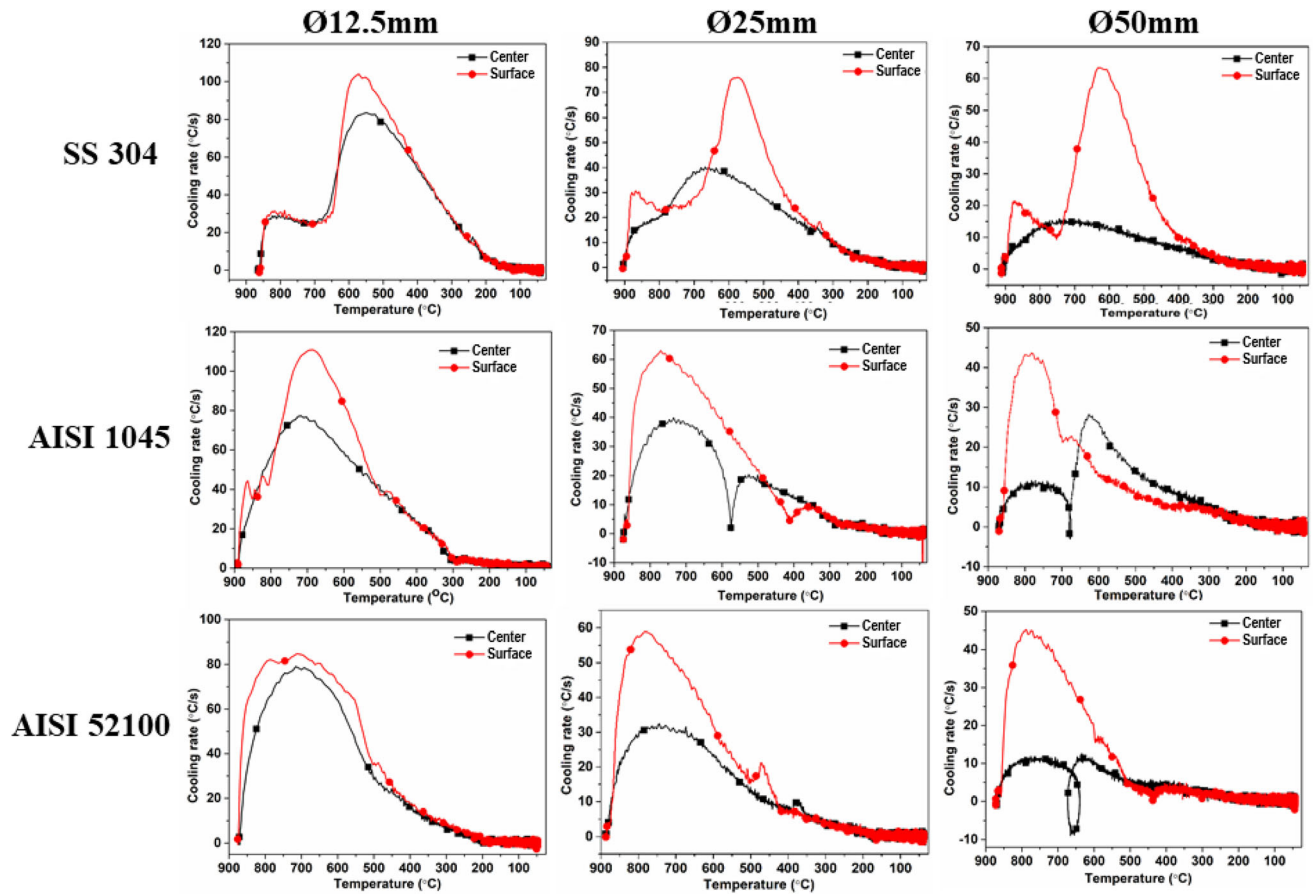
Fig. 7—Curves of cooling rate *vs* temperature measured at the geometric center and 2 mm from the surface of steel probes made of SS 304, AISI 1045, and 52100 with various section thicknesses, respectively, when quenched in mineral oil.

region below 200 °C, where the heat flux flattens, indicates convective cooling. With SS 304 probes, it is observed that increasing probe section thickness increases the magnitude of peak heat flux. The increase in the peak heat flux with the increase in the section thickness is mainly attributed to the increase in the net heat quantity due to the increase in the specimen volume.

The effect of section thickness on the heat flux of AISI 1045 and 52100 steels indicates a reverse trend compared to SS 304. In steels undergoing phase transformation during quenching, the magnitude of peak heat flux decreased with the increase in the diameter of the probe. The phase transformation of austenite into product phases leads to the occurrence of two critical thermo-physical events: (i) liberation of latent heat and (ii) increase in specific heat. The liberation of latent heat causes an instantaneous reheating of the specimen due to the evolved heat, whereas the increase in the specific heat offers resistance to heat dissipation by decreasing the thermal diffusivity $\left(\alpha = \frac{k}{\rho C_p} \right)$ of the steel sample. The amount of latent heat evolution and the magnitude of the increase in the heat capacity increases with the increase in the section thickness of the specimen as the

available volume of austenite for phase transformation increases. As discussed earlier, the film boiling stage is absent in the heat flux plots of AISI 1045 and 52100 steels. The initial peak in the heat flux is due to the nucleate boiling phenomena. The occurrence of phase transformation is observed as a dip and rise in the heat flux thereafter.

Figure 9 compares the heat flux *vs* time data with and without phase transformation. SS 304 indicates the heat flux without phase transformation. Since austenite remains stable in SS 304 steel over the entire temperature range during quenching (from 860 °C to room temperature), the heat flux obtained with SS 304 can be considered a reference, reflecting the heat flux pattern without phase transformation. The heat flux estimated with AISI 1045 (Figure 9(a)) and 52100 (Figure 9(b)) steels represents the heat flux with phase transformation. To quantify the additional heat flux resulting from phase transformation, in Figure 9, the heat flux transients of SS 304 were superimposed on that of AISI 1045 and 52100 steels, respectively, such that the nucleate boiling peaks are coinciding. Figure 8 shows the additional heat liberated due to phase transformation. Without phase transformation, the heat flux curve would have followed an exponential decrease over time
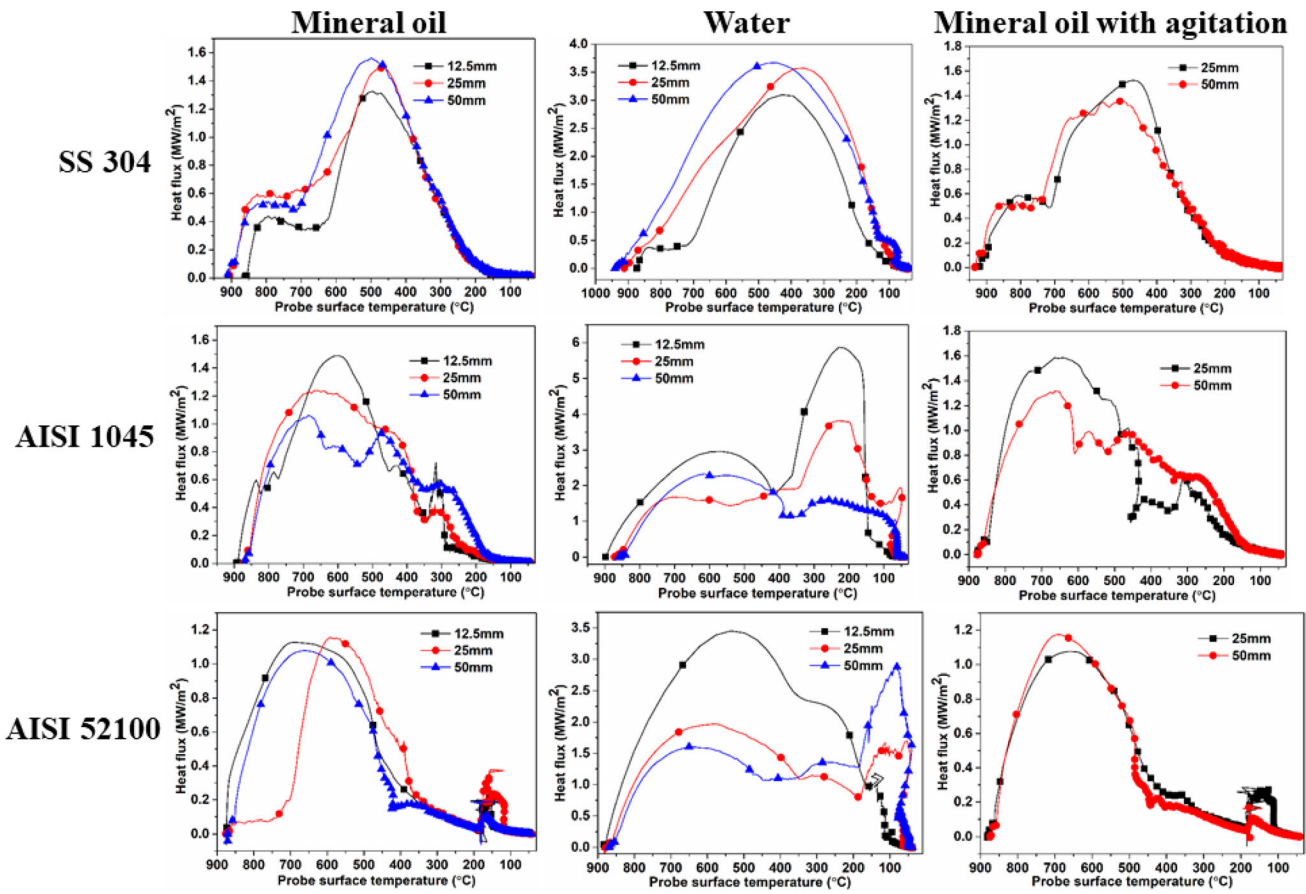
Fig. 8—Comparison of surface heat flux for steel probes of various section thicknesses, including grades SS 304, AISI 1045, and AISI 52100, quenched in mineral oil, water, and agitated mineral oil, respectively.
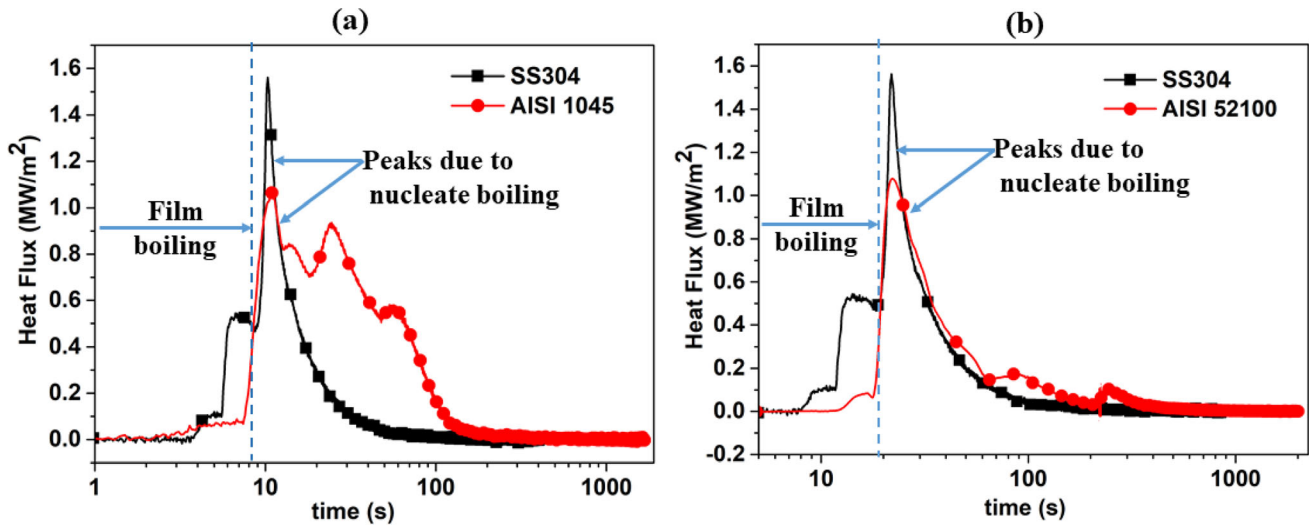

Fig. 9—Comparison of surface heat flux *vs* time with and without phase transformation while quenching 50-mm-diameter steel probes in mineral oil: (*a*) AISI 1045/SS 304, and (*b*) AISI 52100/SS 304.
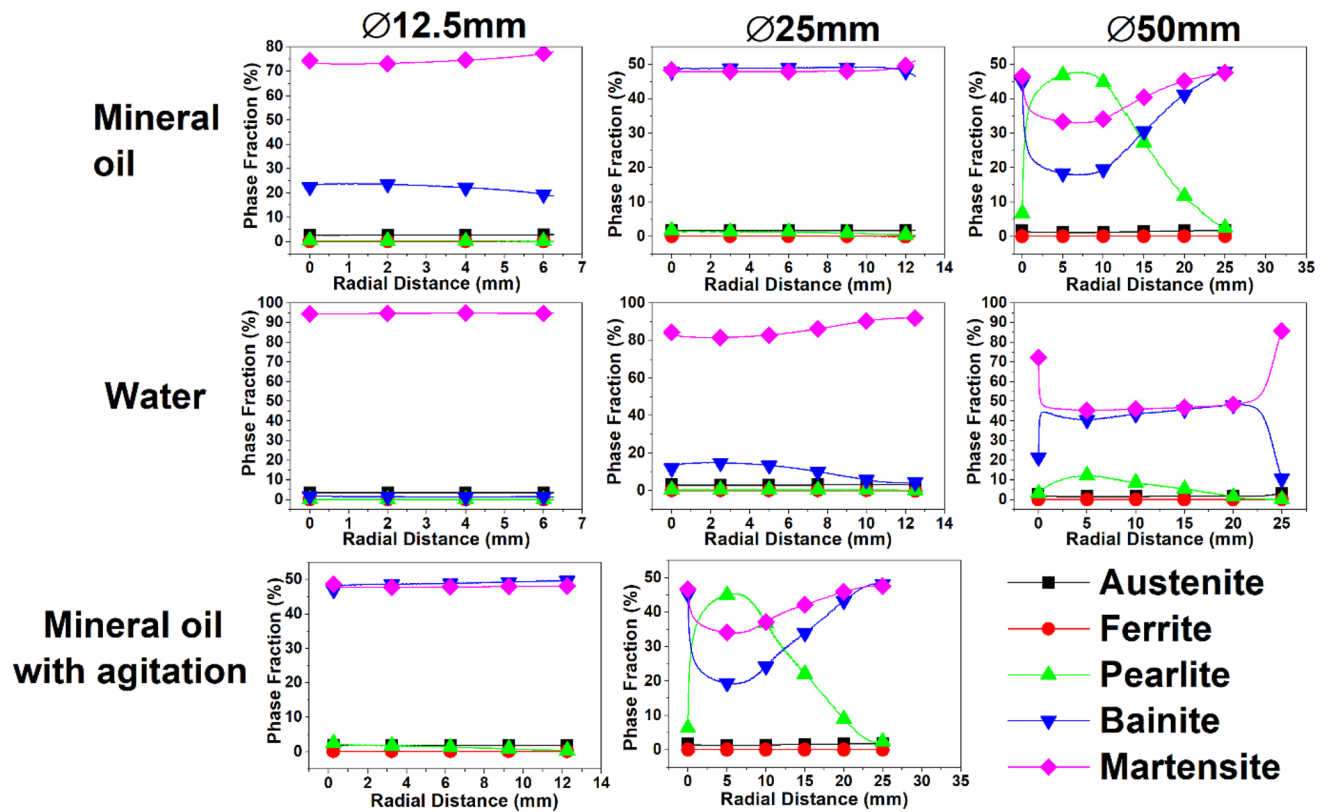
Fig. 10—Radial distribution of phases in AISI 1045 steel probes of diameters 12.5, 25, and 50 mm quenched in mineral oil, water, and agitated mineral oil, respectively.

after reaching its peak value. The effect of phase transformation alters the path followed by the heat flux curve, resulting in dip and rise in heat flux transients after the initial nucleate boiling peak.

C. *Prediction of Microstructure*

The simulation model follows a stage-wise decomposition of austenite into product phases. The ferrite phase forms between Ae3 and Ae1, pearlite between Ae1 and Bs, bainite between Bs and Ms, and martensite thereafter. The only limitation of the model is that it does not accurately predict the formation of the ferrite phase as the transformation range (between Ae1 and Ae3) is very narrow, as observed in the TTT diagram of AISI 1045 steel (Figure 5).

The micro-constituents' phase fractions in the product phases are calculated using the JMAK and KM equations. The fractions related to diffusion-based transformations (austenite to ferrite, pearlite, and bainite) are determined using a combination of Schiel's additive rule and the JMAK equation. The KM equation is employed to calculate the phase fraction of martensitic transformation. The converged heat flux value obtained from the IHCP model at each time step is utilized to externally solve the heat conduction equation. This process is employed to track the temperature

distribution and the phase fractions of the transformed phases at each node of the 1D model during the estimation of transient heat flux.

The radial distribution of phases in the as-quenched probes are shown in Figures 10 and 11 for the AISI 1045 and 52100 steel probes, respectively. The phase fractions are expressed in terms of percentage. Figure 10 shows the distribution of phases in the AISI 1045 steel of various section thicknesses quenched in mineral oil, water and agitated mineral oil, respectively. The medium-carbon steel probes (AISI 1045) quenched in mineral oil showed bainite and pearlite phases along with martensite. The Ø12.5 mm probe showed martensite as the major product phase, along with a smaller phase fraction of bainite. In Ø25 mm, the phase fractions of bainite and martensite are equal. In the case of the Ø50mm probe, a pearlite phase is observed along with bainite and martensite. While quenching in water, martensite is observed to be the primary product phase. The Ø12.5 mm probe shows about 90 pct martensite formation. In the Ø25 and Ø50 mm probes quenched in water, the bainite phase is observed along with martensite. In addition, about 10 pct of the pearlite phase is observed in the Ø50 mm probe. Like the mineral oil, the Ø25 probe quenched in agitated mineral oil showed an equal amount of bainite and martensite.
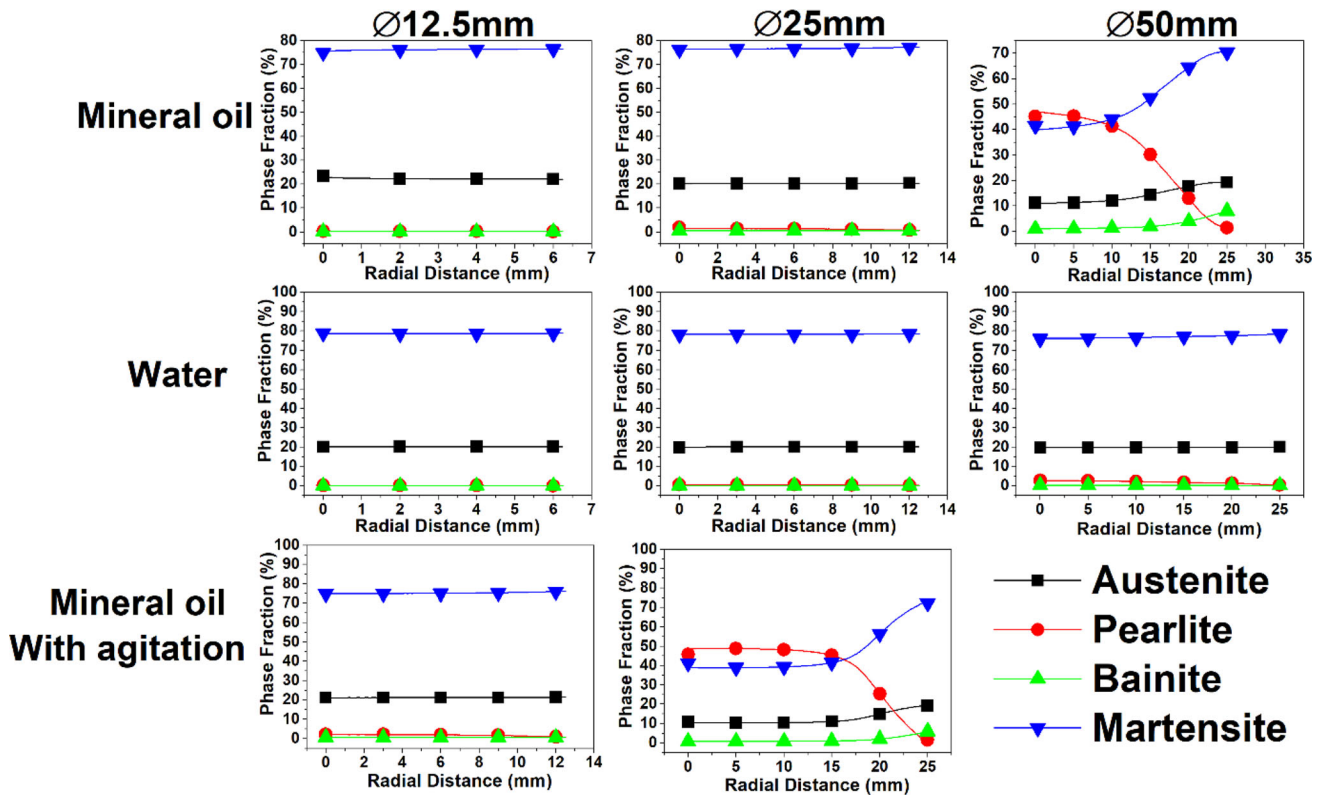
Fig. 11—Radial distribution of phases in AISI 52100 steel probes of diameters 12.5, 25, and 50 mm quenched in mineral oil, water, and agitated mineral oil, respectively.
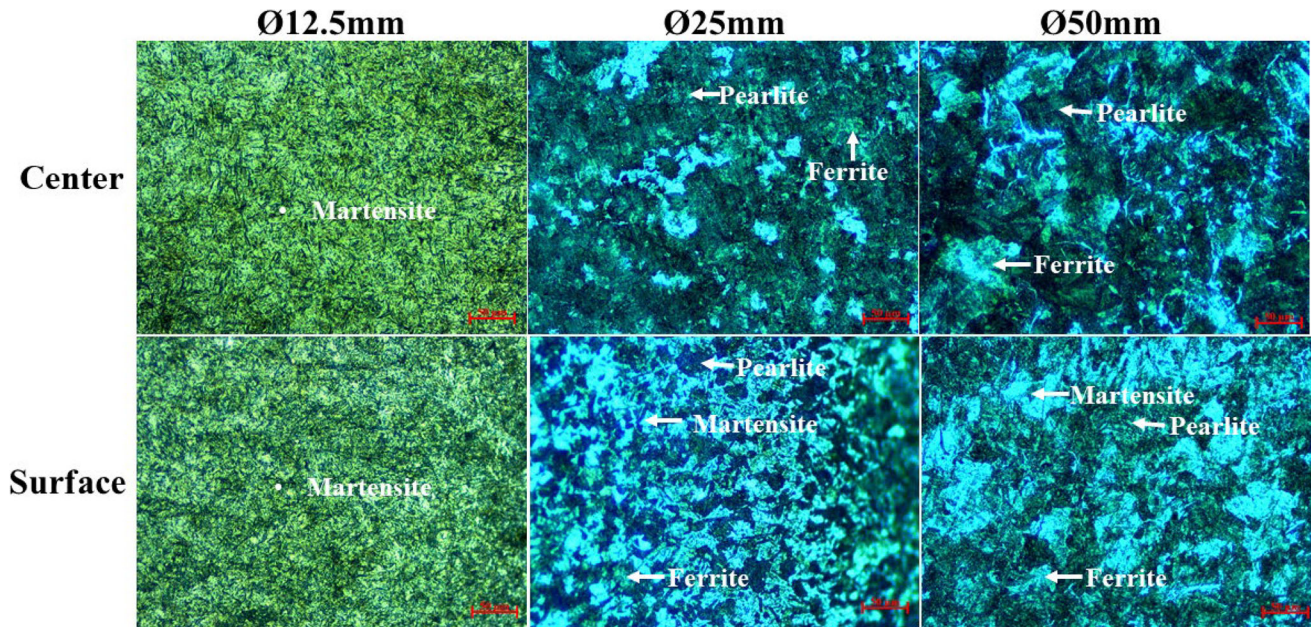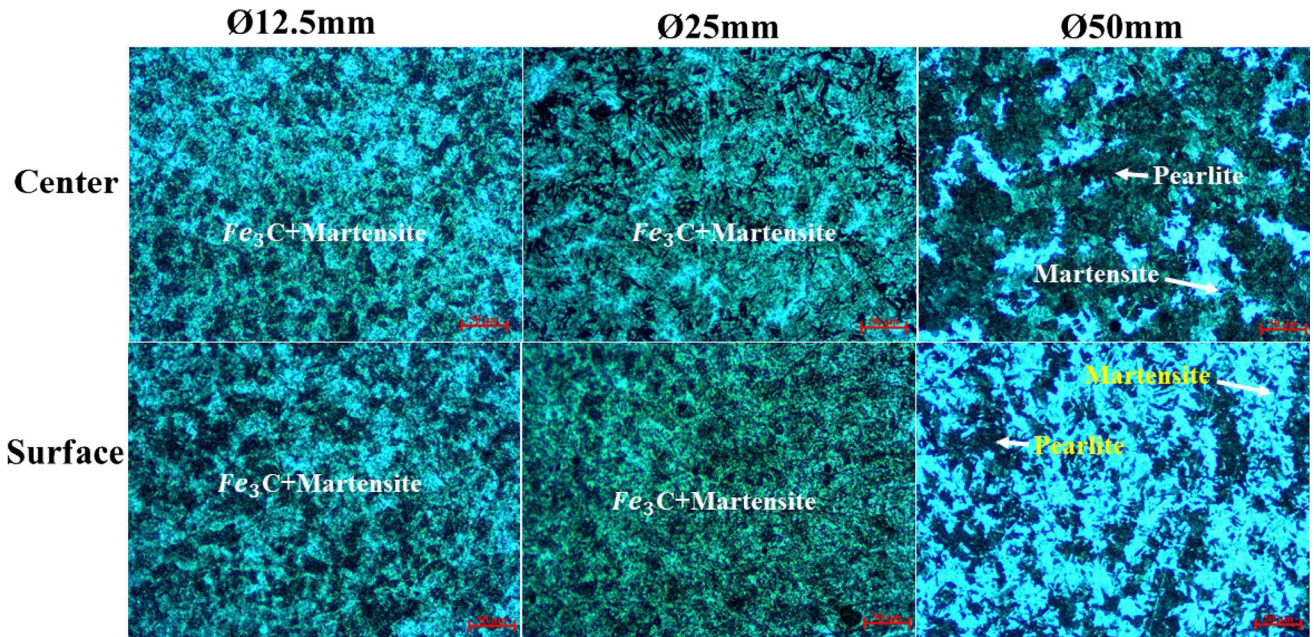

Fig. 12—Microstructure obtained at the geometric center and near the surface of AISI 1045 steel probes of diameters 12.5, 25, and 50 mm, respectively, quenched in mineral oil.

In contrast, the Ø50 mm probe indicated the significant phases of pearlite, bainite, and martensite. The radial distribution of phases in the as-quenched AISI 52100 probes of various section thicknesses quenched in mineral oil, water, and agitated mineral oil, respectively,

are shown in Figure 11. In the case of AISI 52100 probes, the martensite and untransformed austenite are the phases observed in the as-quenched condition in the Ø12.5 and Ø25 mm probes. An exception is the Ø50 mm probe quenched in mineral oil and agitated mineral oil,

Fig. 13—Microstructure obtained at the geometric center and near the surface of AISI 52100 steel probes of diameters 12.5, 25, and 50 mm, respectively, quenched in mineral oil.
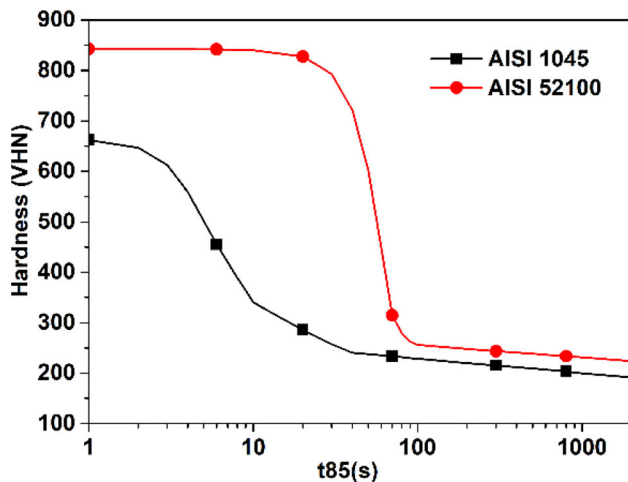
Fig. 14—t85-Hardness correlation (JMAT-Pro).

where a significant amount of pearlite is observed at the center of the probe.

Figures 12 and 13 show microstructures of various section thickness AISI 1045 and 52100 steel probes, respectively, quenched in mineral oil. The microstructures are taken at the center and the surface of the probes. In AISI 1045 steel (Figure 12), a martensitic structure is observed in the Ø12.5 mm probe at the center and surface. A significant amount of ferrite, and pearlitic structure is observed in the center of Ø25 and 50 mm probes, while the surface shows a mixed martensite microstructure with ferrite and pearlite. In the case of AISI 52100 steel quenched in mineral oil (Figure 13), martensite and untransformed austenite were the significant phases observed in Ø12.5 and 25 mm steel probes. The pearlitic structure was observed in the Ø50 mm

probe. Similarly, optical micrographs of AISI 1045 and 52100 steel probes quenched in water and agitated mineral oil are provided in Appendix A5 through A8. The microstructure indicates that the martensite as the significant phase in the Ø12.5 mm probe. As the diameter is increased, the ferrite and pearlitic microstructure is observed predominantly at the center of the steel probe.

D. Validation of Estimated Metal/Quenchant Interfacial Heat Flux

To validate the estimated surface heat flux, the hardness of the as-quenched steel probes was predicted using the simulated temperature distribution and compared with the measured hardness. The hardness of the quenched steel probes was determined using the t85 vs Vickers hardness correlation, as shown in Figure 14, obtained from the JMAT-Pro software. The parameter t85 is the time required for the steel probe to cool from 800 to 500 °C. The t85 is calculated at every node point of the 1D model using the transient temperature distribution obtained using the estimated surface heat flux from the IHCP model. The hardness is interpolated at every node using the t85 vs hardness material correlation.

Figures 15 compare the predicted hardness with the measured hardness of the AISI 1045 and 52100 steel probes of various section thicknesses quenched in mineral oil, water, and agitated mineral oil, respectively. The predicted hardness agrees with the measured hardness for Ø25 and Ø50 mm probes quenched in mineral oil, water, and agitated mineral oil, respectively. However, the predicted hardness was underestimated in the case of Ø12.5 mm probes quenched in mineral oil and water. The underestimation of hardness is
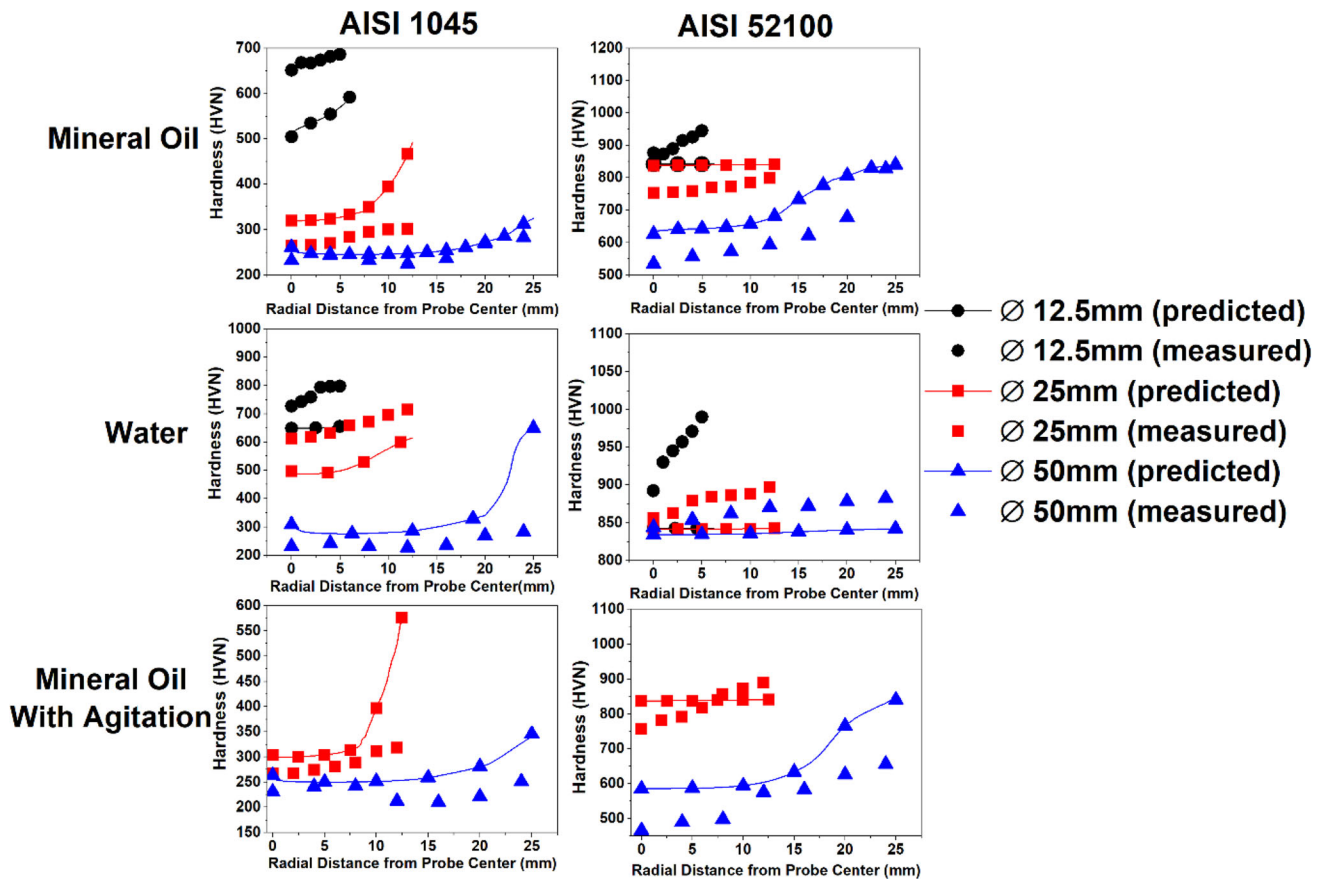
Fig. 15—Comparison of simulated hardness with the measured hardness for AISI 1045 and 52100 steel probes of various section thicknesses, quenched in mineral oil, water, and agitated mineral oil, respectively.

attributed to the limitations of the t85 *vs* hardness correlation. The t85 *vs* hardness provides fairly accurate prediction when the hardness ranges from 150 to 670 HVN in the case of AISI 1045 steel and 180 to 850 HVN in the case of AISI 52100 steels.

E. Error Analysis with Temperature as the Boundary Condition at the Center of the Probe FE Model

The temperature recorded at the center of the probe is used as the boundary condition in the 1D FE model to improve the temperature prediction accuracy, which is essential for achieving an accurate prediction of transformed phases. Figure 16 shows the percentage error between the measured temperature and the estimated temperature at the center of the probe when the center temperature boundary condition is not specified in the IHCP model. The figure indicates that an error of 7, 15, and 25 pct is observed at the center for AISI 1045 steel probes with Ø12.5, 25, and 50 mm diameters, respectively, quenched in mineral oil. It was observed that an increase in probe section thickness increases the temperature prediction error at the center. This is mainly due to the time lag or the delay in the phase transformation at the surface and the center of the probe, which increases with the increase in probe section thickness. As a result, the accuracy of the prediction of temperature
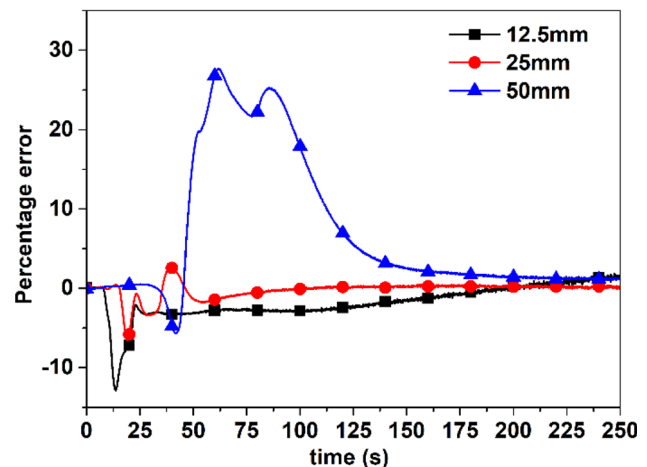

Fig. 16—Percentage error between the measured and estimated temperature at the geometric center of AISI 1045 steel probes of diameters 12.5, 25, and 50 mm, respectively, while quenching in mineral oil.

distribution by the inverse method decreases. However, for stainless steel probes, where there is no phase transformation involved, the percentage error of temperature prediction was not more than 3 pct, even with increased probe diameter.
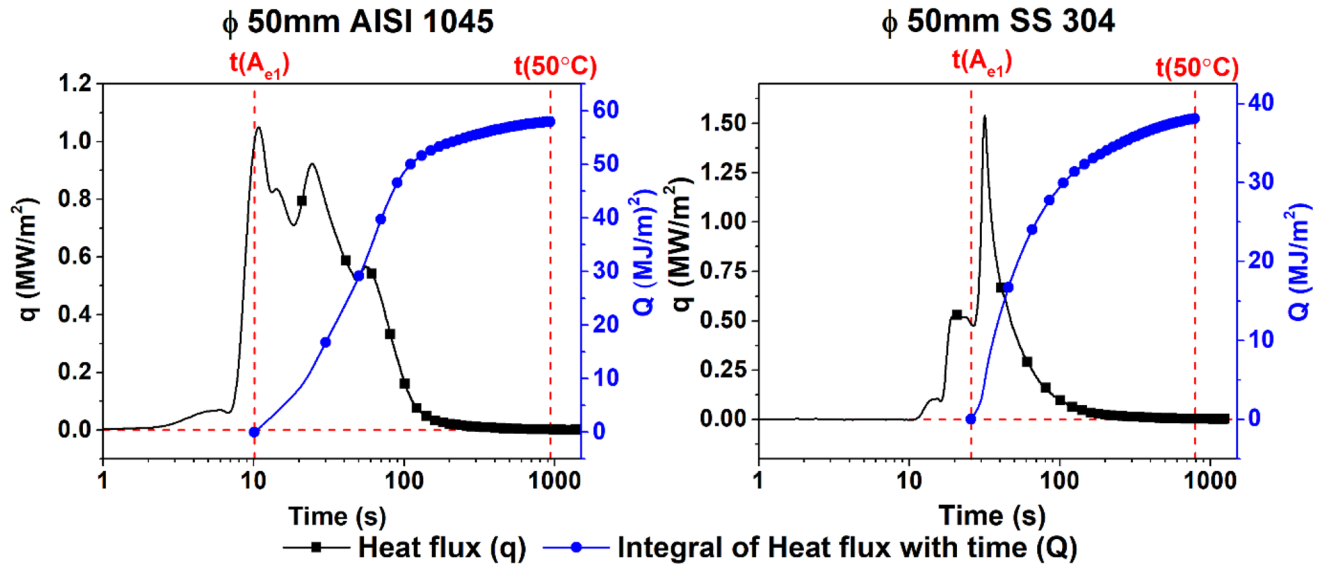
Fig. 17—Deriving integral of heat flux (Q) from estimated surface heat flux *vs* time data in 50-mm-diameter steel probes of AISI 1045 and SS 304 indicating the heat flux with and without phase transformation, respectively.

F. *Estimation of Phase Transformation Enthalpy Parameter (ΔQ)*

A phase transformation enthalpy parameter (ΔQ) was proposed to quantify the additional heat lost to the quench medium due to phase transformation in the steel probe. The parameter ΔQ is defined as the difference in the heat lost from the steel to the quenchant with and without phase transformation and is calculated per unit weight to generalize the net heat quantity for various shapes and sizes of steel. Figure 17 shows the surface heat flux as a function of time for Ø50 mm probes of AISI 1045 and SS 304, respectively, quenched in mineral oil. The integral of heat flux or the total amount of heat lost to the quenchant from the probe surface is determined by integrating the heat flux (q) for time (t) as shown in the equation below.

$$Q = \int_{t(A_{e1})}^{t(50)} q \, \mathrm{d}t \qquad [35]$$

The limits of the integration $t(A_{e1})$ and $t(50)$ indicate the times corresponding to the surface temperature corresponding to the start of transformation, which is taken as A_{e1} and 50 °C, respectively. Since an appreciable amount of ferrite was not observed in the simulated phase distribution, the starting of transformation was considered from A_{e1} and not A_{e3} for AISI 1045 probes. In the case of AISI 52100 probes, A_{e1} temperature is chosen as the start of transformation instead of A_{cm}. It is assumed that in 52100 steel probes, 0.94 wt pct cementite phase is already existing at the austenitizing temperature (860 °C), and the remaining austenite (99.02 wt pct) is transformed into either pearlite, bainite, or martensite depending on the rate of cooling.

The amount of heat loss (Q) is of the unit joule per square meter (J/m^2). To convert the amount of heat loss into joule per unit weight (J/kg), Q is multiplied by the lateral surface area of the probe and divided by the weight, as shown in the equation below. D and L in the equation are the diameter and length of the probe, respectively.

$$Q\left(\frac{J}{\mathrm{kg}}\right) = Q\left(\frac{J}{\mathrm{m^2}}\right) \frac{\pi D L}{\textit{weight of probe} \ (\mathrm{kg})} \qquad [36]$$

Since the top and bottom parts of the probe are insulated, it is assumed that the heat transfer is unidirectional and occurs only through the lateral surface area of the probe. The weights of the steel probes were found to be 0.057, 0.114, and 0.455 kg for Ø12.5, 25, and 50 mm probes, respectively. Figure 18 compares the heat lost per unit weight of the steel probes. Figure 18(a) compares the heat loss per unit weight for Ø50mm AISI 1045 and SS 304 probe, while Figure 18(b) compares the heat loss for Ø50mm AISI 52100 and SS 304 probe. Compared to the heat loss in the SS 304 probe, the medium- and high-carbon steel probes show increased heat loss. The additional amount of heat lost is the enthalpy change due to the effect of phase transformation. Finally, ΔQ is calculated as a function of temperature by subtracting heat loss per unit weight of AISI 1045 and 52100 steels from that of SS 304 steel probes of their respective diameters.

$$\Delta Q_{\mathrm{steel}}(T) = Q_{\mathrm{steel}}(T) - Q_{SS304}(T) \qquad [37]$$

The parameter ΔQ was calculated similarly for Ø12.5 and 25 mm probes of both steels quenched in mineral oil, water, and agitated mineral oil. A nonlinear curve fitting was performed to obtain a best-fit curve that indicates the ΔQ irrespective of section thickness for a particular steel grade. Figure 19 shows the regression fit of ΔQ for AISI 1045 and 52100 steel probes, of various section thicknesses, quenched in various quench media.

A good fit was observed in the case of AISI 1045 steel probes. The goodness of fit indicated by R^2 was about 0.94 for mineral oil and agitated mineral oil, whereas the goodness of fit for water was about 0.9. For 52100 probes, the goodness of fit was about 0.82 and 0.83 for mineral oil and agitated mineral oil, respectively, while water showed a lower correlation of 0.75. It should be noted that the method proposed to calculate ΔQ is subject to experimental and computational errors. The reference probe, SS 304, used to obtain the heat flux without phase transformation, shows an initial film boiling stage, whereas the heat flux of steel probes having phase transformation does not show any film boiling during quenching. The difference in the steel/quenchant interface heat transfer phenomena can induce errors in calculating ΔQ. Therefore, the proposed method is reasonably accurate and can be further refined.

ΔQ was quantified as a function of probe temperature using the following equation,

$$\Delta Q = A_2 + \frac{(A_1 - A_2)}{\left(1 + \left(\frac{T}{T_o}\right)^p\right)} \qquad [38]$$
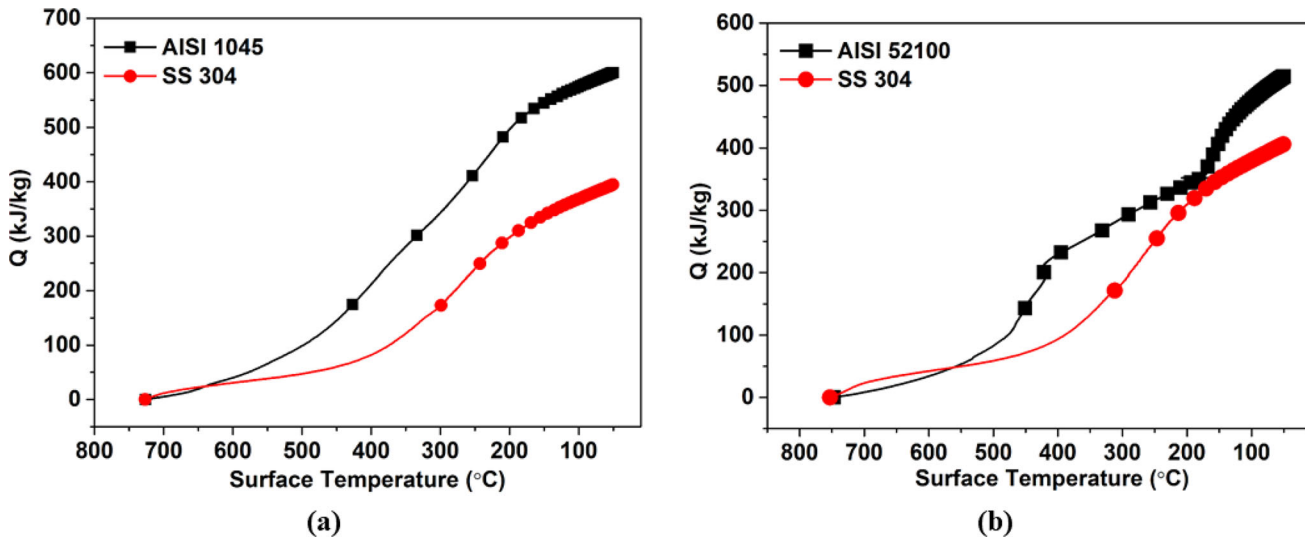

Fig. 18—Heat liberated per unit weight of the steel probes while quenching in mineral oil for 50-mm-diameter steel probes: (a) AISI 1045/SS 304 and (b) AISI 52100/SS 304.
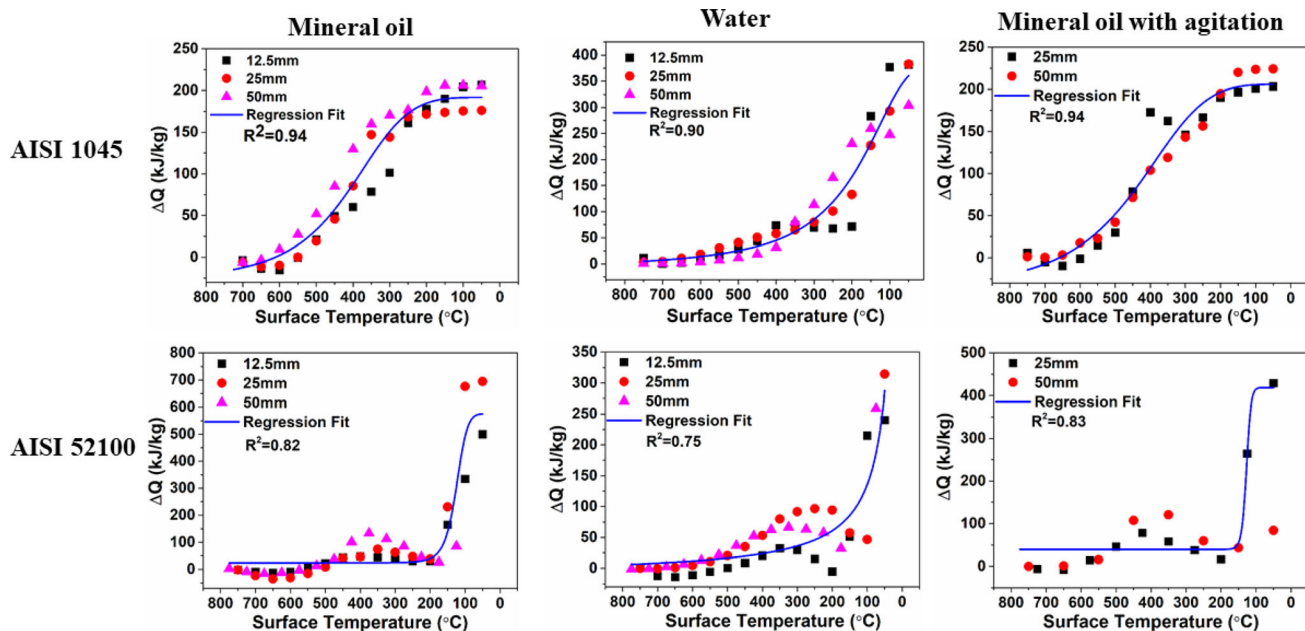

Fig. 19—ΔQ for AISI 1045 and 52100 steel probes while quenching in mineral oil, water, and agitated mineral oil, respectively.

Table III.   Constants of ΔQ Empirical Equation for AISI 1045 Steel

Constants	Mineral Oil		Water		Agitated Mineral Oil	
	Value	Std. Deviation	Value	Std. Deviation	Value	Std. Deviation
A_1	191.93	4.55	376.95	25.36	205.96	6.18
A_2	− 28.16	11.0	− 8.35	13.75	− 38.66	19.76
T_o	408.85	12.5	185.38	13.0	438.95	22.16
p	4.76	0.60	2.37	0.39	4.09	0.67

Table IV.   Constants of ΔQ Empirical Equation for AISI 52100 Steel

Constants	Mineral oil		Water		Agitated Mineral Oil	
	Value	Std. Deviation	Value	Std. Deviation	Value	Std. Deviation
A_1	575.65	34.95	138606.36	6.37×10^7	418.63	24.06
A_2	24.38	7.97	− 11.73	28.37	39.38	5.77
T_o	125.70	4.70	0.125	56.81	127.41	3.13
p	7.54	1.72	0.024	0.75	19.10	10.57
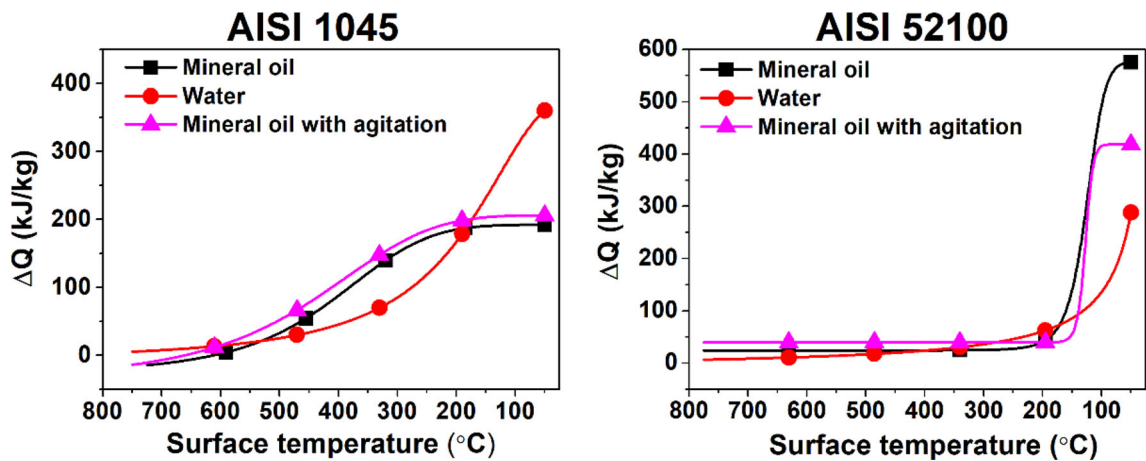
Fig. 20—Comparison of variation of ΔQ with the change in the quenching medium.

where A_1, A_2, T_o, and p are constants of the empirical equation. Tables III and IV show the values of constants of the Eq. [38] for AISI 1045 and 52100 steels quenched in various media.

G. *Effect of Quench Media and Composition of Steel on ΔQ*

Figure 20 shows the variation of ΔQ with quench media for AISI 1045 and 52100 steels. It is observed that for 1045 steel, quenching in mineral oil and agitated mineral oil resulted in a gradual increase of ΔQ with the decrease in the probe surface temperature from A_{e1} to 50 °C. In contrast, water quenching resulted in a steep rise in ΔQ at the start of martensitic temperature. For 52100 steels, a reverse trend was observed. Mineral oil quenching showed a higher magnitude and sharp rise of ΔQ as compared to agitated mineral oil and water. The phase transformation in steels is of two types: (1) diffusion-based, where the austenite is transformed to ferrite, pearlite, and bainite, and (2) diffusion-less transformation, where the austenite transforms to martensite. In the case of mineral oil-quenched 1045 steel probes, diffusion-based transformations are significant alongside the martensitic transformation. The diffusion-based transformation is time-dependent phenomenon and occurs over a period of time. Hence, the ΔQ curve rises gradually with the temperature.

On the other hand, fast cooling in water produces higher phase fraction of martensite and lower phase fractions of diffusion-based transformation. Hence, a steep rise of ΔQ at about martensitic temperature is observed. In the case of 52100 steel, martensite is the significant transformation occurring in mineral oil and water. Hence, the ΔQ remains minimum until a temperature of 200 °C and a rise in ΔQ is observed thereafter.

IV. CONCLUSIONS

- Metal/quenchant interfacial heat flux transients showed a dip and rise due to the effect of phase transformation.
- Without phase transformation, increasing the section thickness of the steel increases the surface heat flux, whereas, with phase transformation, the magnitude of surface heat flux decreases with the increase in section thickness. This was caused by the liberation of latent heat and the decrease in the thermal diffusivity of the steel probe owing to a rise in the specific heat.
- The hardness predicted by the phase transformation-coupled IHCP model was in good agreement with the measured hardness indicating that the inverse model is accurate in estimating steel/quenchant interfacial heat flux with phase transformation.
- A phase transformation enthalpy parameter (ΔQ) during quenching was proposed to characterize the enthalpy change during phase transformations during quenching of different grades of steels with varying section thickness. ΔQ incorporates the difference in the thermophysical properties and the liberation of latent heat due to phase transformation. The parameter ΔQ was found to be the same for a particular steel grade and is independent of the section thickness of the component. However, ΔQ was found to vary with cooling rates or the type of the quench medium.
- The incorporation of phase transformation in the quenching heat transfer model is complex due to the vast material data inputs, such as the TTT/CCT diagrams and thermophysical properties of steel that vary with the steel grade. The vast material data input required for quenching simulation makes it complex in nature. Incorporating ΔQ in the phase transformation-coupled heat conduction equation or the IHCP minimizes the material data input and thus simplifies the simulation process. A database of ΔQ as a function of temperature and cooling rate would ease modeling of heat transfer during quench hardening.

CONFLICT OF INTEREST

The authors declare that they have no conflict of interest.

APPENDIX
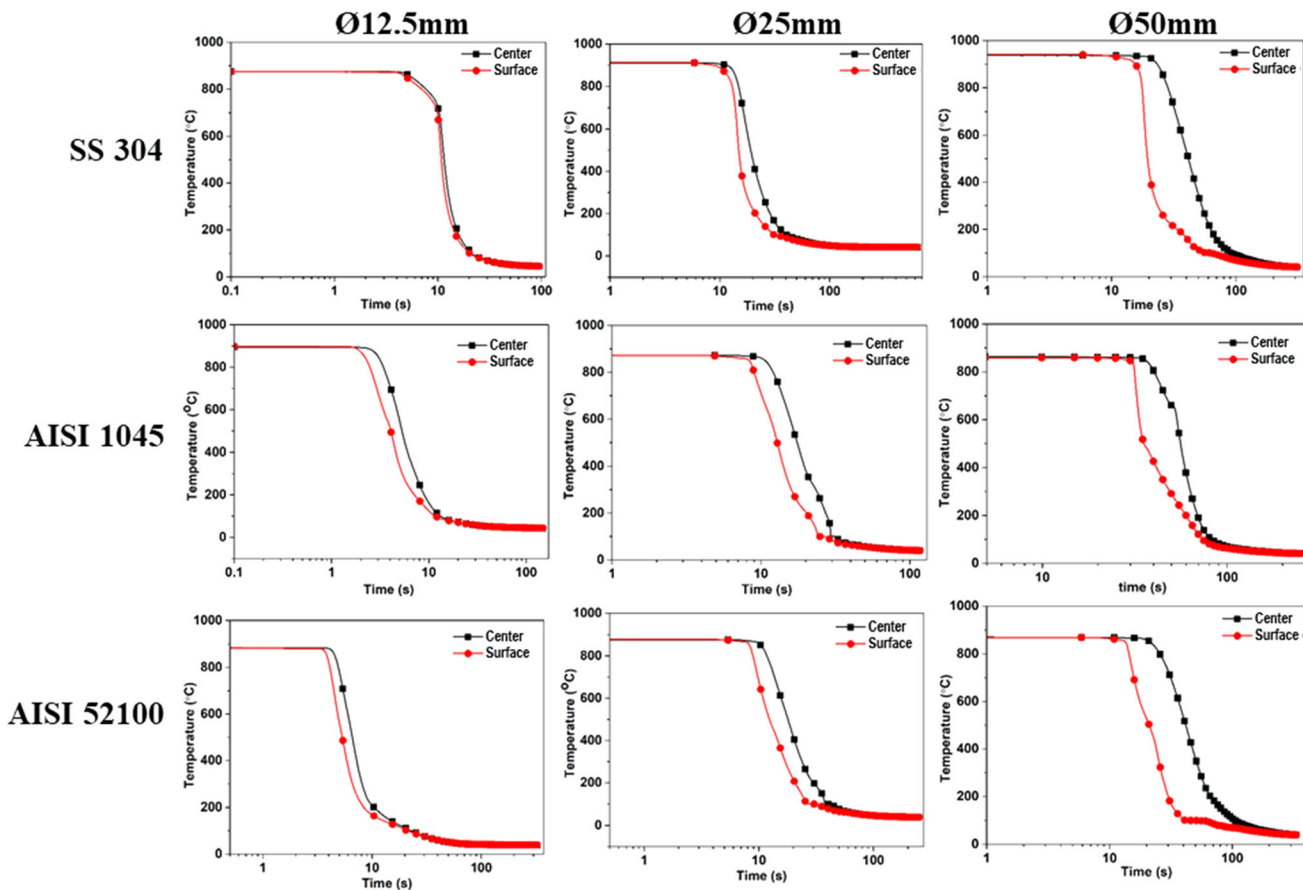
See Figures A1, A2, A3, A4, A5, A6, A7, A8.

Fig. A1—Temperature *vs* time profiles measured at the geometric center and 2 mm from the surface of various section thickness SS 304, AISI 1045 and 52100 steel probes, respectively, quenched in water.
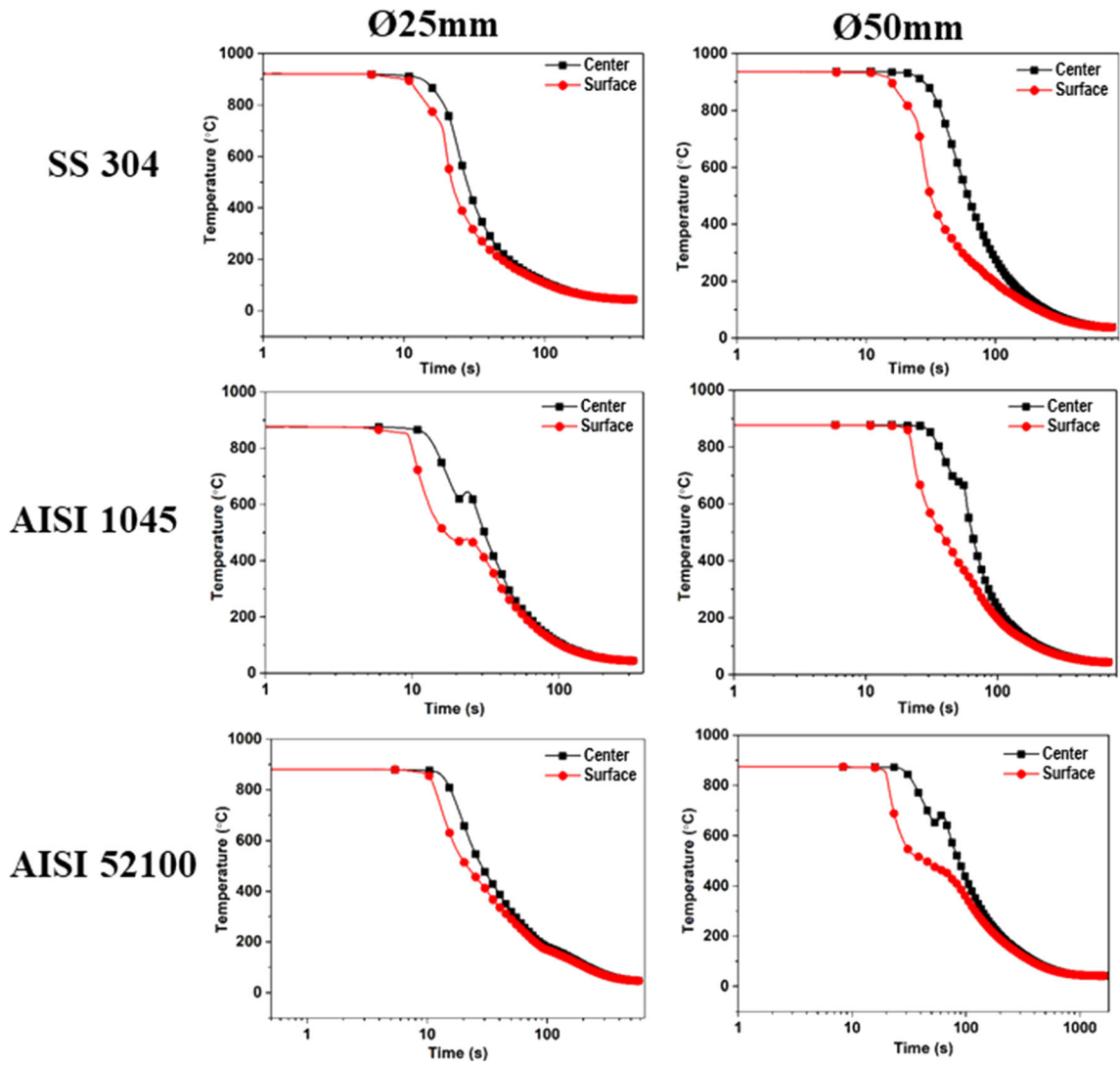
Fig. A2—Temperature *vs* time profiles measured at the geometric center and 2 mm from the surface of various section thickness SS 304, AISI 1045 and 52100 steel probes, respectively, quenched in agitated mineral oil.
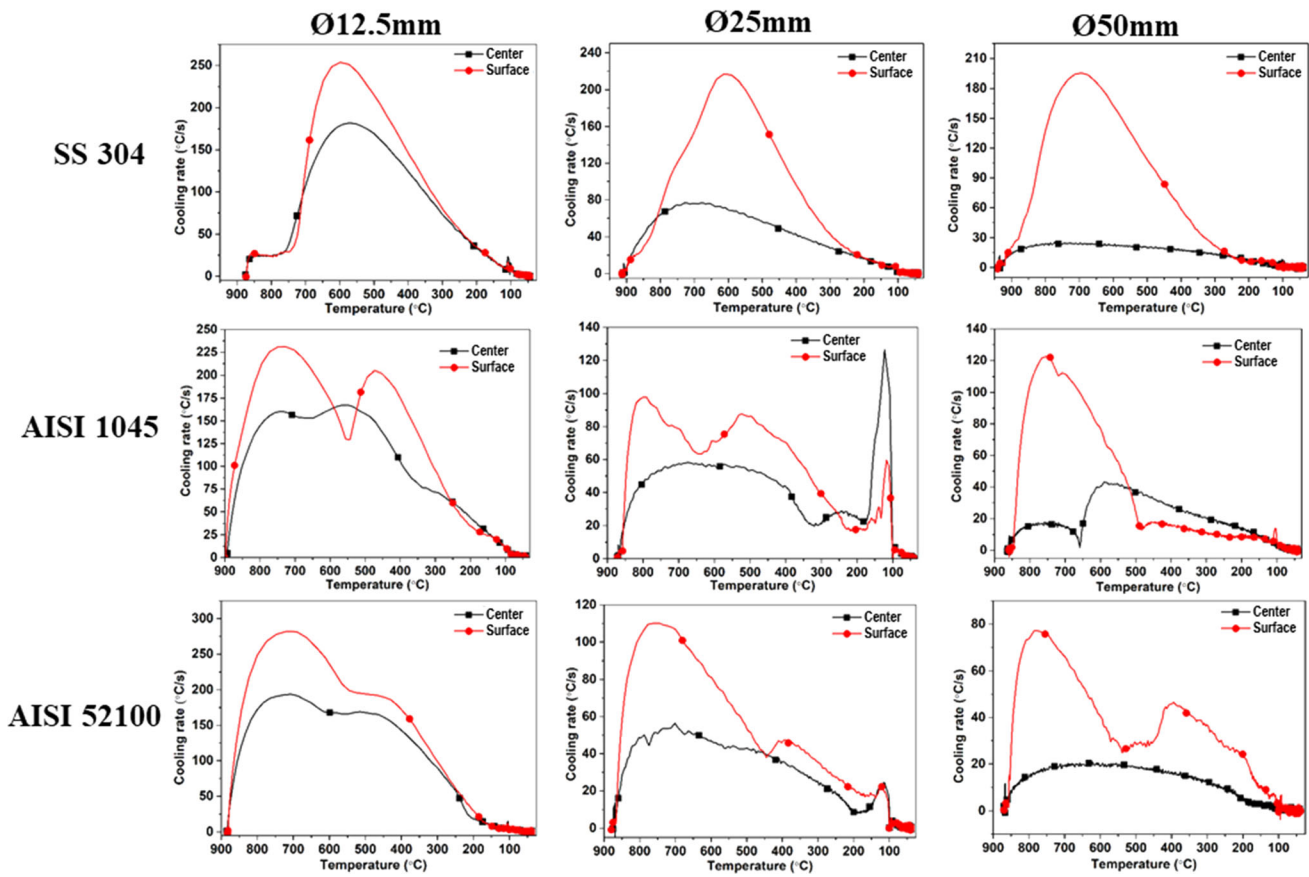
Fig. A3—Curves of cooling rate *vs* temperature measured at the geometric center and 2 mm from the surface of steel probes made of SS 304, AISI 1045 and 52100 with various section thicknesses, respectively, when quenched in water.
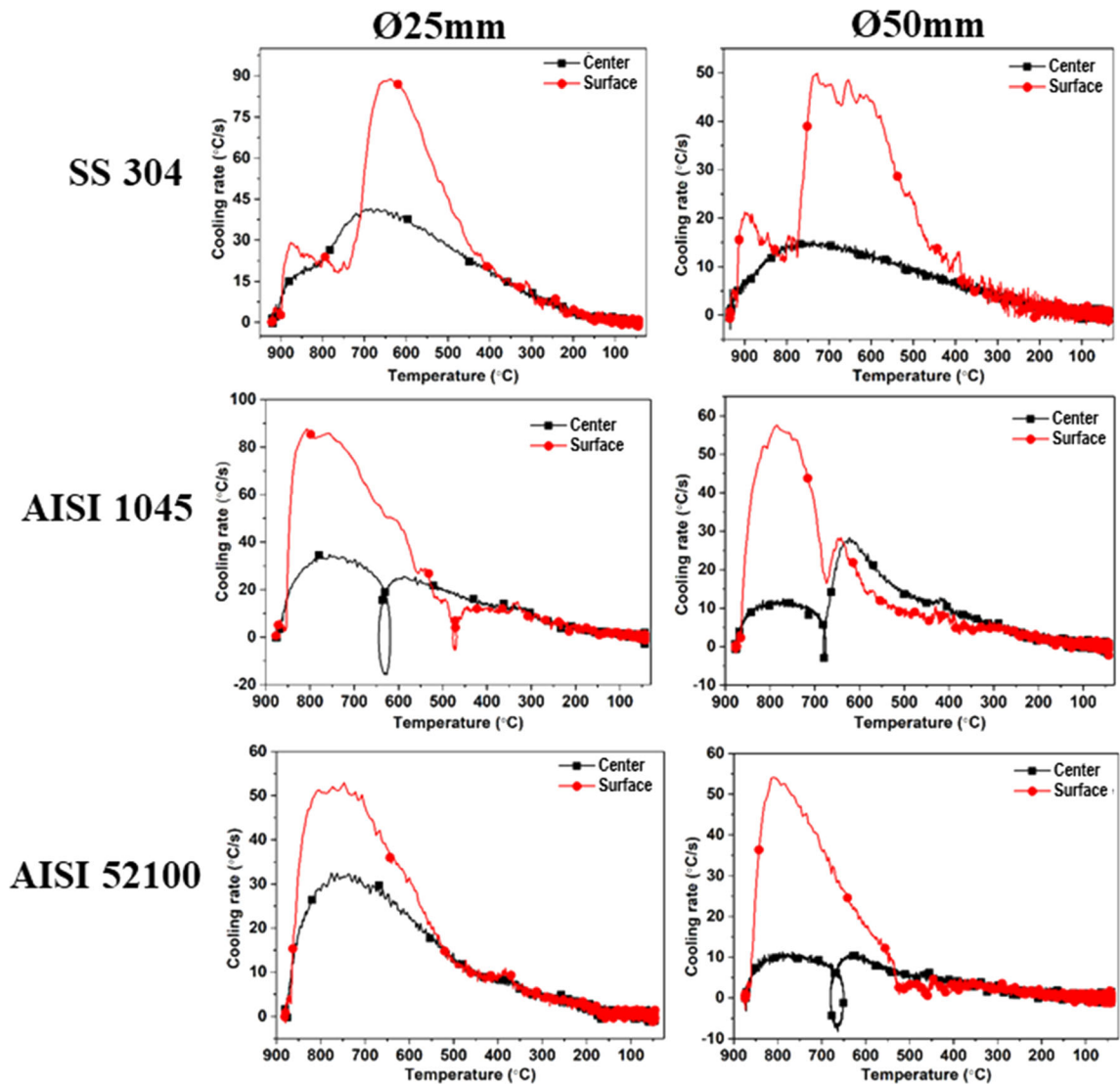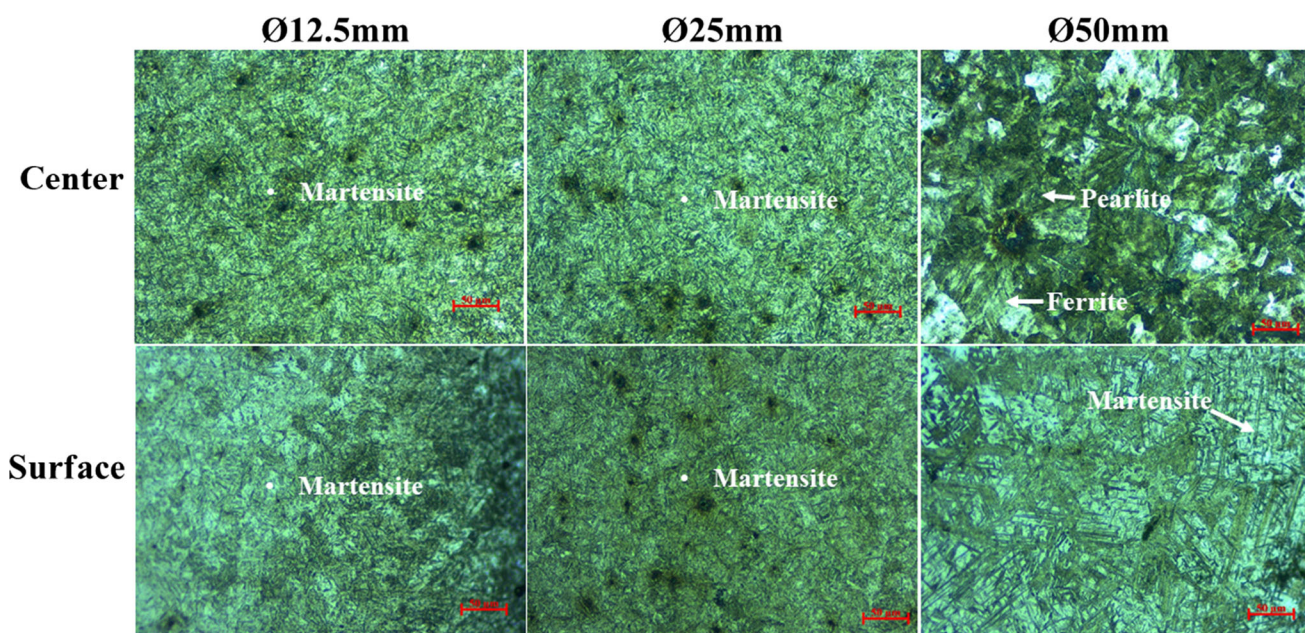
Fig. A4—Curves of cooling rate *vs* temperature measured at the geometric center and 2 mm from the surface of steel probes made of SS 304, AISI 1045 and 52100 with various section thicknesses, respectively, when quenched in agitated mineral oil.

Fig. A5—Microstructure obtained at the geometric center and near the surface of AISI 1045 steel probes of diameters 12.5, 25, and 50 mm, respectively, quenched in water.
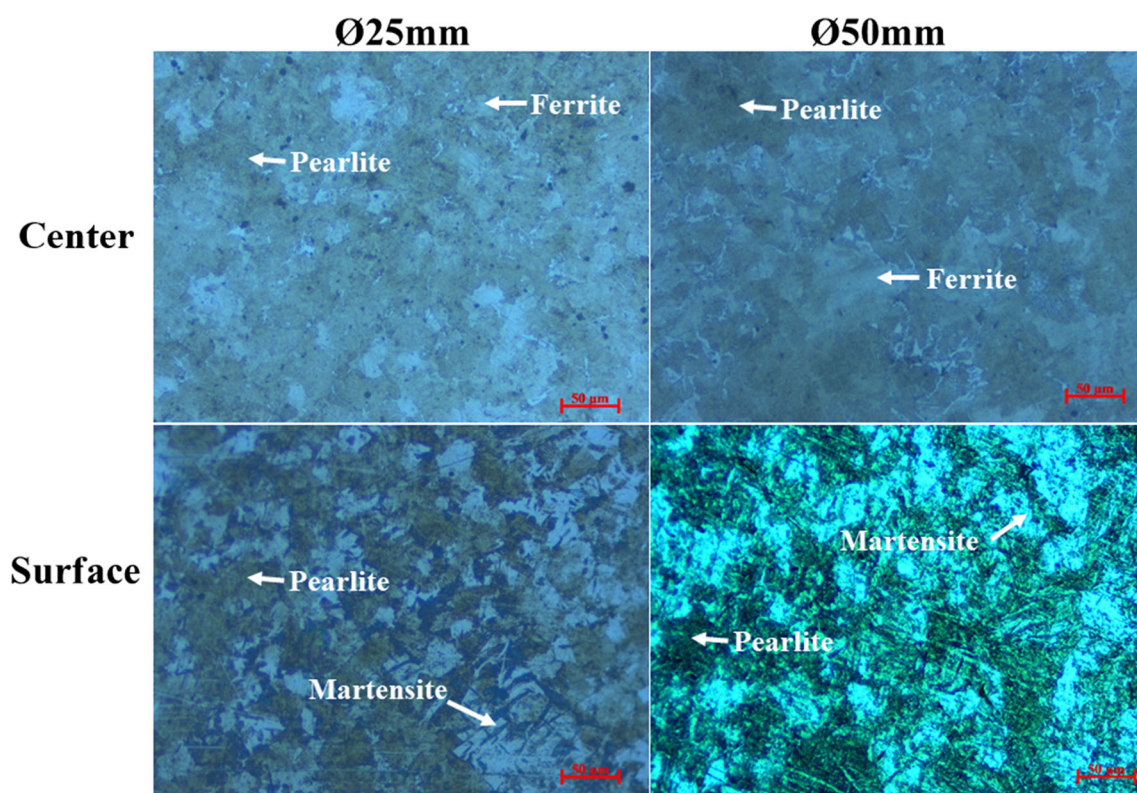

Fig. A6—Microstructure obtained at the geometric center and near the surface of AISI 1045 steel probes of diameters 12.5, 25, and 50 mm, respectively, quenched in agitated mineral oil.
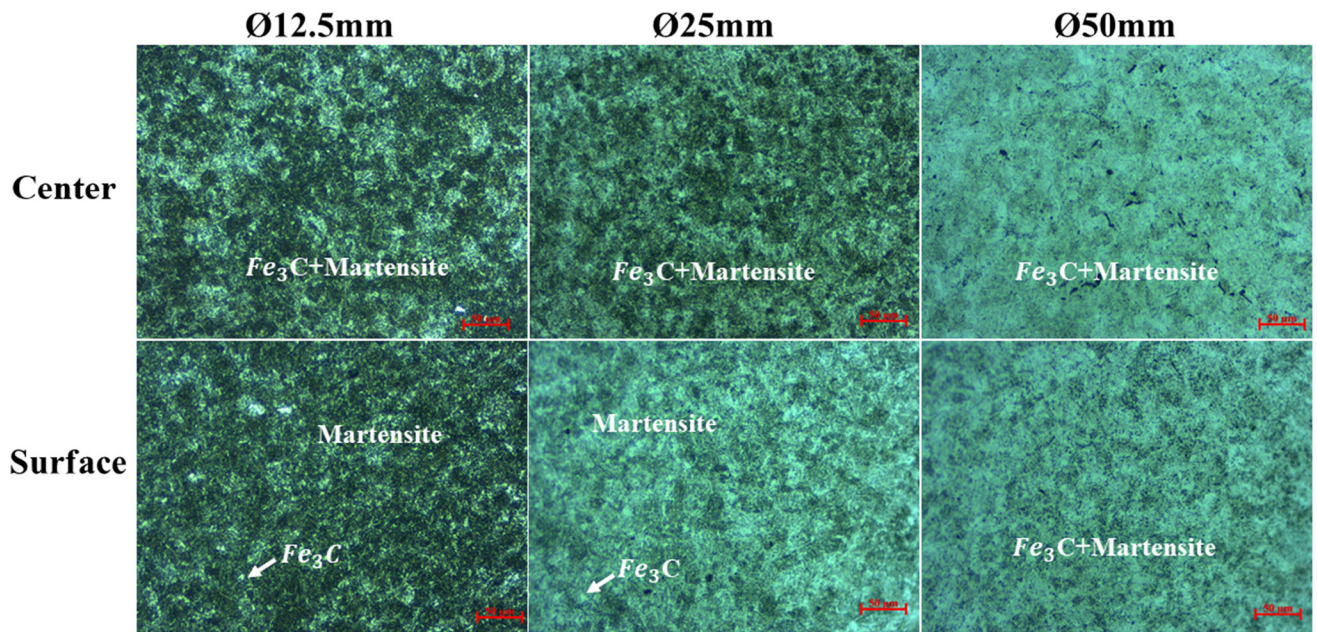
Fig. A7—Microstructure obtained at the geometric center and near the surface of AISI 52100 steel probes of diameters 12.5, 25, and 50 mm, respectively, quenched in water.
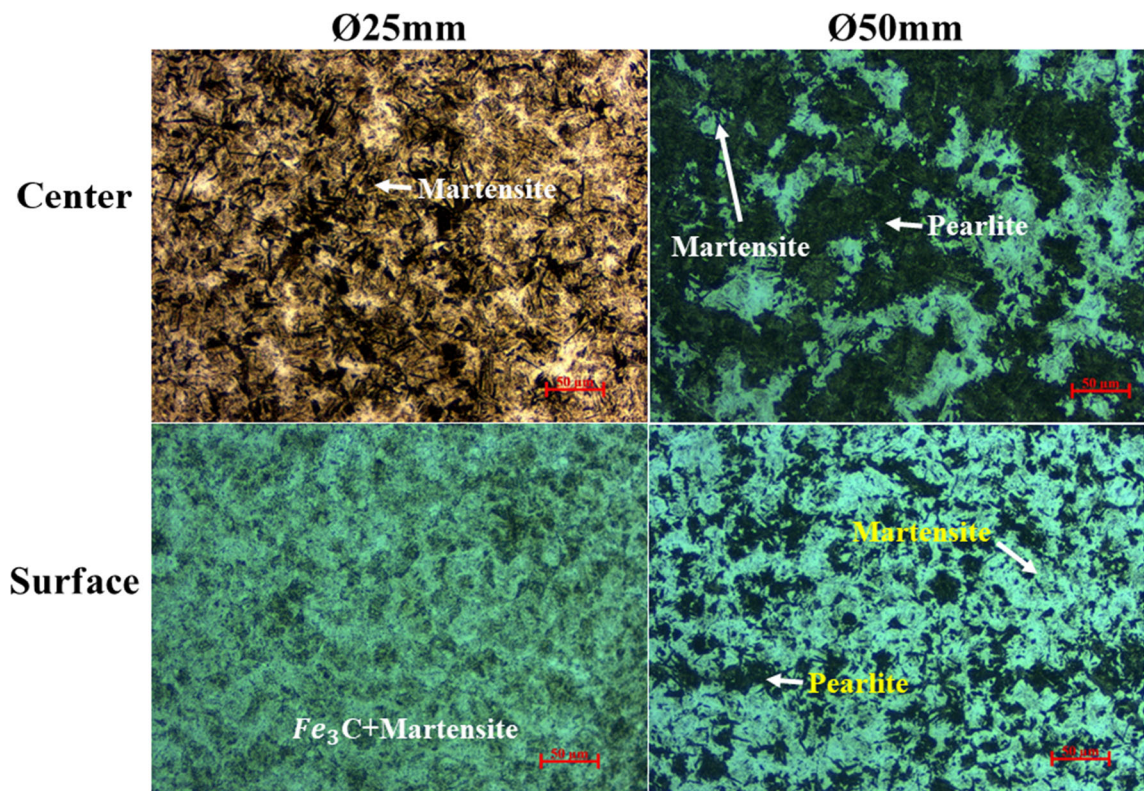

Fig. A8—Microstructure obtained at the geometric center and near the surface of AISI 52100 steel probes of diameters 12.5, 25, and 50 mm, respectively, quenched in agitated mineral oil.

NOMENCLATURE

A_{e3}	Critical temperature for austenite–ferrite transformation (°C)
A_{e1}	Critical temperature for austenite–pearlite transformation (°C)
A_{cm}	Critical temperature for austenite–cementite transformation (°C)
B_s	Critical temperature for austenite–bainite transformation (°C)
C_p	Specific heat capacity (J/kgK)
D/Ø	Diameter (m)
IHCP	Inverse Heat Conduction Problem
k	Thermal conductivity (W/mK)
L	Length (m)
M_S	Critical temperature for austenite–martensite transformation (°C)
m	Mass/weight (kg)
q	Heat flux (W/m^2)
Q	Amount of heat (J)
r	Radius (m)
ρ	Density (kg/m^3)
t	Time (s)
T	Temperature (°C)
TTT	Time–temperature transformation
ΔT	Temperature difference (°C)
V	Volume (m^3)

REFERENCES

1. C. Simsir and C.H. Gur: in *Quenching Theory and Technology*, B. Liscic, H.M. Tensi, L.C.F. Canale, and G.E. Totten, eds., Second., CRC Press, 2010, pp. 605–68.
2. A. Samuel and K.N. Prabhu: *J. Mater. Eng. Perform.*, 2022, vol. 31, pp. 5161–88.
3. C. Simsir and C.H. Gur: in *Handbook of Thermal Process Modeling Steels*, C.H. Gur and J. Pan, eds., CRC Press, 2009, pp. 341–426.
4. J. Jan and D.S. MacKenzie: *J. Mater. Eng. Perform.*, 2020, vol. 29, pp. 3612–25.
5. G. Ramesh and K. Narayan Prabhu: *Heat Mass Transf.*, 2015, vol. 51, pp. 11–21.
6. K.M.P. Rao and K.N. Prabhu: *J. Mater. Eng. Perform.*, 2020, vol. 29, pp. 3494–3501.
7. R. Jeschar, E. Specht, and C. Köhler: in *Quenching Theory and Technology*, B. Liscic, H.M. Tensi, L.C.F. Canale, and G.E. Totten, eds., Second., CRC Press, 2010, pp. 159–78.
8. G. Ramesh and K.N. Prabhu: *Heat Transf. - Asian Res.*, 2016, vol. 45, pp. 342–57.
9. G.E. Totten, H.M. Tensi, and L.C.F. Canale: in *Proc. 22nd Heat Treat. Sco. Conf. 2nd Int. Surf. Eng. Congr.*, ASM International, Indianapolis, 2003, pp. 148–54.
10. R. Gopalan and P. Narayan: *Nanoscale Res. Lett.*, 2011, vol. 6, p. 334.
11. C. Simsir and C.H. Gur: *J. ASTM Int.*, 2009, vol. 6, pp. 1–29.
12. B.H. Morales, H.J.V. Hernandez, G.S. Diaz, and G.E. Totten: in *Evaporation, Condensation and Heat transfer*, A. Ahsan, ed., IntechOpen, London, 2011, pp. 49–72.
13. G. Ramesh and K. Narayan Prabhu: *Metall. Mater. Trans. B*, 2016, vol. 47B, pp. 859–81.
14. P. Fernandes and K.N. Prabhu: *J. Mater. Process. Technol.*, 2007, vol. 183, pp. 1–5.
15. J. Grum, S. Božič, and M. Zupančič: *J. Mater. Process. Technol.*, 2001, vol. 114, pp. 57–70.
16. G. Ramesh and K. Narayan Prabhu: *Mater. Perform. Charact.*, 2012, vol. 1, pp. 1–8.
17. K. Babu: *Adv. Mater. Res.*, 2012, vol. 488–489, pp. 353–57.
18. U.V. Nayak and K.N. Prabhu: *Mater. Perform. Charact.*, 2018, vol. 7, pp. 384–96.
19. T.S. Prasanna Kumar: *J. Mater. Eng. Perform.*, 2013, vol. 22, pp. 1848–54.
20. G.E. Totten, C.E. Bates, and N.A. Clinton: *Handbook of Quenchants and Quenching Technology*, ASM International, Materials Park, 1993.
21. J.V. Beck: *Int. J. Heat Mass Transf.*, 1970, vol. 13, pp. 703–16.
22. S. Das and A.J. Paul: *Metall. Trans. B*, 1993, vol. 24, pp. 1077–86.
23. K.N. Prabhu and A.A. Ashish: *Mater. Manuf. Process.*, 2002, vol. 17, pp. 469–81.
24. K. Babu and T.S.P. Kumar: *Metall. Mater. Trans. B*, 2010, vol. 41B, pp. 214–24.
25. T.S. Prasanna Kumar: *Mater. Perform. Charact.*, 2012, vol. 1, pp. 1–22.
26. K. Babu and T.S. Prasanna Kumar: *Metall. Mater. Trans. B*, 2014, vol. 45B, pp. 1530–44.
27. N.R.A. Simha, M.P. Sushanth, V.B. Sachin, Maruti, T.S.P. Kumar, and V. Krishna: *Met. Sci. Heat Treat.*, 2019, vol. 61, pp. 448–54.
28. M.N. Ozisik and H.R.B. Orlande: *Inverse Heat Transfer: Fundamentals and Applications*, Taylor & Francis, New York, 2000.
29. C. Simsir and C.H. Gur: in *Handbook of Thermal Process Modeling Steels*, C.H. Gur and J. Pan, eds., CRC Press, 2008, pp. 341–426.
30. A. Samuel, U.V. Nayak, K.M.P. Rao, and K.N. Prabhu: in *Proceedings of the HT 2023. Heat Treat 2023: Proceedings from the 32nd Heat Treating Society Conference and Exposition.*, Detroit, MI, 2023, pp. 88–97.
31. JMAT Pro, https://www.sentesoftware.co.uk/jmatpro, (accessed 16 June 2023).